

# Effect of component separation on the temperature distribution of the CMB

R.B. Barreiro<sup>1</sup>, E. Martínez-González<sup>1</sup>, P. Vielva<sup>1,2</sup> and M.P. Hobson<sup>3</sup>

<sup>1</sup>*Instituto de Física de Cantabria, CSIC-Universidad de Cantabria, Santander, Spain*

<sup>2</sup>*PCC - Collège de France, 11, place Marcelin Berthelot, F-75231 Paris, France*

<sup>3</sup>*Astrophysics Group, Cavendish Laboratory, Madingley Road, Cambridge CB3 0HE*

Accepted —. Received —; in original form 12 June 2018

## ABSTRACT

We present a study of the effect of component separation on the recovered cosmic microwave background (CMB) temperature distribution, considering Gaussian and non-Gaussian input CMB maps. In particular, the non-Gaussian maps have been generated as a mixture of a Gaussian CMB map and a cosmic strings map in different proportions. First, we extract the CMB component from simulated multifrequency Planck data (in small patches of the sky) using the maximum-entropy method (MEM), Wiener filter (WF) and a method based on the subtraction of foreground templates plus a linear combination of frequency channels (LCFC). We then apply a wavelet-based method to study the Gaussianity of the recovered CMB and compare it with the same analysis for the input map. When the original CMB map is Gaussian (and assuming that point sources have been removed), we find that neither MEM nor WF introduce non-Gaussianity in the CMB reconstruction. Regarding the LCFC, the Gaussian character is also preserved provided that the appropriate combination of frequency channels is used. On the contrary, if the input CMB map is non-Gaussian, all the studied methods produce a reconstructed CMB with lower detections of non-Gaussianity than the original map. This effect is mainly due to the presence of instrumental noise in the data, which clearly affects the quality of the reconstructions. In this case, MEM tends to produce slightly higher non-Gaussian detections in the reconstructed map than WF whereas the detections are lower for the LCFC. We have also studied the effect of point sources in the MEM reconstruction. If no attempt to remove point sources is performed, they clearly contaminate the CMB reconstruction, introducing spurious non-Gaussianity. When the brightest point sources are removed from the data using the Mexican Hat Wavelet, the Gaussian character of the CMB is preserved. However, when analysing larger regions of the sky, the variance of our estimators will be appreciably reduced and, in this case, we expect the point source residuals to introduce spurious non-Gaussianity in the CMB distribution. Therefore a careful subtraction (or masking) of point source emission is crucial in order to be able to perform Gaussian analysis of the CMB.

**Key words:** methods: data analysis, techniques: image processing, cosmic microwave background

## 1 INTRODUCTION

One of the most valuable tools of modern cosmology is the observation and analysis of anisotropies in the cosmic microwave background (CMB) radiation. A number of experiments such as Boomerang (Netterfield et al. 2002), MAXIMA (Hanany et al. 2000), DASI (Halverson et al. 2002), VSA (Grainge et al. 2003), CBI (Mason et al. 2003), ACBAR (Kuo et al. 2004), Archeops (Benoit et al. 2003) and WMAP (Bennett et al. 2003a) have already provided

measurements of the power spectrum of the CMB, allowing one to put tight constraints on the cosmological parameters. In addition, the temperature distribution of the CMB also carries crucial information about the theory of structure formation. In particular, the standard inflationary theory predicts Gaussian fluctuations for the CMB whereas topological defect models (Turok & Spergel 1990, Durrer 1999) and non-standard inflation (Linde & Mukhanov 1997, Peebles 1997, Bernardeau & Uzan 2002, Acquaviva et al.

arXiv:astro-ph/0503039v2 24 Mar 2006

2003, Bartolo et al. 2004) introduce non-Gaussian signatures on the cosmological signal. Therefore, a detection of intrinsic non-Gaussianity in the CMB would have far reaching consequences for the current understanding of cosmology.

When observing the microwave sky, however, one measures not only the cosmological signal but a mixture of the CMB with other contaminant components. The most important of these are the emissions from our own Galaxy (mainly synchrotron, free-free and dust emission), the thermal and kinematic Sunyaev-Zeldovich effects and the emission from extragalactic point sources. In addition, the data will also be corrupted by instrumental noise and possibly some systematic effects. Therefore, in order to extract all the valuable information encoded in the CMB, it is critical to separate the cosmological signal from the other microwave components. This is especially relevant for the success of future CMB experiments, which will measure the microwave sky with unprecedented resolution, sensitivity, sky and frequency coverage. Most notably, these include the WMAP mission by NASA (that will continue to take data in the next few years) and the Planck mission by ESA (to be launched in 2007), both of which produce all-sky multifrequency observations of the CMB. The problem of component separation is a particularly important issue in the analysis of the temperature distribution of the CMB, since foregrounds and/or systematics may well introduce non-Gaussian signatures on the cosmological signal or, conversely, impair our ability to detect underlying intrinsic non-Gaussianity. The component separation process itself should also be well understood in order to avoid the introduction of artifacts that can modify the temperature distribution of the CMB.

The study of the Gaussianity of the CMB has recently attracted a great interest with the release of the 1st-year WMAP data (Bennett et al. 2003a). There have been many analyses of the temperature distribution of the CMB (Komatsu et al. 2003, Colley & Gott 2003, Gaztañaga & Wagg 2003, Gaztañaga et al. 2003, Chiang et al. 2003, Eriksen et al. 2004a,b, Park 2004, Magueijo & Medeiros 2004, Vielva et al. 2004, Copi, Huterer & Starkman 2004, Hansen et al. 2004, Mukherjee & Wang 2004, Larson & Wandelt 2004, Coles et al. 2004, Schwarz et al. 2004, Cabella et al. 2005, Chiang & Naselsky 2004, Cruz et al. 2005, McEwen et al. 2005, Land & Magueijo 2005, Cayón, Jin & Treaster 2005) and, although for some of them the data are consistent with Gaussian fluctuations, in other cases there has been a detection of non-Gaussianity and/or asymmetries, whose origin can not always be attributed to the presence of foregrounds or systematics. For instance, Vielva et al. (2004) use a method based on the spherical Mexican Hat wavelet (MHW) and claim a non-Gaussian detection outside the 99 per cent acceptance region, for which an intrinsic origin can not be discarded. By extending the analysis method to orientable spherical wavelets, McEwen et al. (2005) also obtained a significant non-Gaussian detection.

With regard to the component separation problem, several methods have been proposed in the literature. There are basically two different approaches. The first one is to design a method to extract only a particular component from the microwave sky. The second one attempts to reconstruct all the components at the same time. The

first approach is particularly well suited to the extraction of compact sources (for a review see e.g. Barreiro 2006), such as the emission from extragalactic point sources or the thermal and kinematic Sunyaev-Zeldovich (SZ) effects. Such methods include the use of the MHW (Cayón et al. 2000, Vielva et al. 2001a,b, 2003) the matched filter (Tegmark & de Oliveira-Costa 1998, Herranz et al. 2002a, Pierpaoli 2003, Schulz & White 2003, López-Caniego et al. 2004, Herranz et al. 2005, Schaefer et al. 2004, Melin, Bartlett & Delabrouille 2005), the scale-adaptive filter (Sanz, Herranz & Martínez-González 2001, Herranz et al. 2002a,b,c, Barreiro et al. 2003), the adaptive top-hat filter (Chiang et al. 2002), the biparametric scale adaptive filter (López-Caniego et al. 2005a,b), the Bayesian approach proposed by Diego et al. (2002), the McClean algorithm (Hobson & McLachlan 2003) or the wavelet-based method of Pierpaoli et al. (2005). In addition, there are methods that try to extract only the CMB component from the data, such as the blind EM algorithm of Martínez-González et al. (2003) or the internal linear combination method (Bennett et al. 2003b, Tegmark, de Oliveira-Costa & Hamilton 2003, Eriksen et al. 2004c). Regarding the techniques that attempt to separate and reconstruct all the components at the same time, we have Wiener filter (WF, Bouchet et al. 1996; Tegmark & Efstathiou 1996), the maximum-entropy method (MEM, Hobson et al. 1998, 1999a, Stolyarov et al. 2002, 2005, Barreiro et al. 2004, Bennett et al. 2003b) or blind source separation (Baccigalupi et al. 2000, Maino et al. 2002, 2003, Delabrouille, Cardoso & Patanchon 2003, Bedini et al. 2005, Patanchon et al. 2005).

The effect that these techniques have on the recovered power spectrum of the CMB have been studied in many of the cases. However, no attention has been paid to the effect that the component separation may have on the underlying CMB temperature distribution. As already mentioned, the Gaussianity of the CMB fluctuations is predicted by the standard inflationary model and, therefore, a detection of intrinsic non-Gaussianity would have a great impact on our current knowledge of the universe. Thus, a complete understanding of the processing of the data is crucial since otherwise we could either misidentify spurious non-Gaussian signatures as true ones or impair our ability to detect intrinsic non-Gaussianity. In the present work, we will study the effect of some component separation techniques on the underlying CMB temperature distribution. In order to do this, first we will apply different component separation techniques (MEM, WF, combined MEM+MHW and a linear combination of the frequency channels, LCFC) to simulated Planck data of small patches of the sky. We will perform then a Gaussianity analysis based on a wavelet technique to the reconstructed CMB map and compare the results with the same analysis for the input map.

The outline of the paper is as follows. In Section 2 we summarise the different component separation methods that are applied in this work. The wavelet technique used for the Gaussian analysis is explained in Section 3 whereas Section 4 describes the Planck simulated data. Our results are given in Section 5 and section 6 presents some additional tests to understand further the role of foregrounds and noise in the

component separation process. Finally a discussion and our conclusions are presented in Sections 7 and 8 respectively.

## 2 COMPONENT SEPARATION TECHNIQUES

In the present section we outline the problem of component separation and briefly describe the techniques used for that purpose in this work. Our aim is to reconstruct the different components of the microwave sky, and in particular the CMB, in the presence of instrumental noise from multifrequency microwave observations.

Let us assume that we are performing a multifrequency observation (at  $n_f$  frequencies) of the microwave sky in a given direction  $\mathbf{x}$ . We will obtain a  $n_f$ -dimensional data vector that contains the observed temperature fluctuations in this direction at each observing frequency, plus instrumental noise. The measured data at the  $\nu$ th frequency in the direction  $\mathbf{x}$  can be written as

$$d_\nu(\mathbf{x}) = \sum_{j=1}^{N_p} B_\nu(|\mathbf{x} - \mathbf{x}_j|) \sum_{p=1}^{n_c} F_{\nu p} s_p(\mathbf{x}_j) + \eta_\nu(\mathbf{x}_j) + \epsilon_\nu(\mathbf{x}), \quad (1)$$

where  $n_c$  denotes the number of physical components to be separated and  $N_p$  is the number of pixels in each map. The function  $B_\nu$  accounts for the instrumental beam and  $\epsilon_\nu(\mathbf{x})$  corresponds to the instrumental noise at frequency  $\nu$  and position  $\mathbf{x}$ . As is usual for the component separation techniques, we make the assumption that each of the components (except point sources) can be factorised into a spatial template ( $s_p$ ) at a reference frequency  $\nu_0$  and a frequency dependence encoded in  $F_{\nu p}$ . Note that point sources can not be factorised in this way since each of them has its own frequency dependence. The term  $\eta_\nu$  includes the emission of this component (convolved with the beam) at each frequency. Therefore, the component separation technique will attempt, at least, to extract the CMB from the data  $d_\nu$  and, possibly, to reconstruct the rest of microwave components as well as a catalogue of point sources at each frequency.

In the next subsections we outline some of the existing methods to perform this component separation. We have considered for this work the maximum-entropy method (MEM), a MEM+MHW joint analysis, the Wiener filter and a method based on the linear combination of frequency channels (LCFC). There are other methods that have been proposed in the literature. For instance, the EM algorithm of Martínez-González et al. (2003), that extracts only the CMB, and SMICA (Dellabrouille et al. 2003), which reconstruct all the components, are blind source approaches that first recover the power spectra of the considered components and then uses this information to form the image using Wiener filter. Therefore they are also, somewhat, included in our study. Another important technique that has been applied to the problem of component separation in the CMB field is FastICA (Maino et al. 2002). Although this method is indeed very promising, some further development to improve the way in which FastICA deals with correlated foreground components, realistic beams and instrumental noise is, however, still needed. For this reason, we have chosen not to include this technique in this first analysis of the effect of component separation on the temperature distribution of the CMB.

### 2.1 The maximum-entropy method

The maximum-entropy method (MEM) has been successfully applied to reconstruct the microwave components from simulated Planck data in a small patch of the sky (Hobson et al. 1998). The algorithm was extended to deal with point sources (Hobson et al. 1999a) and also combined with the Mexican hat wavelet (MHW; Vielva et al. 2001b). Subsequently, MEM has been adapted to work with spherical data at full Planck resolution (Stolyarov et al. 2002). Finally, Stolyarov et al. (2005) have presented an improved MEM algorithm that can accommodate anisotropic noise and spatial spectral variations. All the previous algorithms work in harmonic (or Fourier) space. In addition, Barreiro et al. (2004) developed a MEM algorithm that combines both harmonic and real spaces and that can naturally deal with anisotropic noise and incomplete sky coverage. The method was applied to the COBE data. Bennett et al. (2003b) has also applied a different maximum-entropy based algorithm to the WMAP data.

In this subsection we briefly outline the basics of MEM. For a more detailed derivation, see Hobson et al. (1998, 1999a). If the beam is circularly symmetric and assuming that Fourier modes are independent, it is convenient to work in Fourier space (or harmonic space if dealing with all-sky observations). In this way, the reconstruction can be performed for each mode separately, what greatly simplifies the problem. Using matrix notation; equation (1) can be written for each Fourier mode as

$$\mathbf{d} = \mathbf{R}\mathbf{s} + \boldsymbol{\eta} + \boldsymbol{\epsilon} = \mathbf{R}\mathbf{s} + \boldsymbol{\zeta} \quad (2)$$

where  $\mathbf{d}$ ,  $\boldsymbol{\eta}$  and  $\boldsymbol{\epsilon}$  are column vectors each containing  $n_f$  complex components and  $\mathbf{s}$  is a column vector containing  $n_c$  complex components. The response matrix  $\mathbf{R}$  has dimension  $n_f \times n_c$  and accounts for the effect of the beam and the spectral dependence of each of the components. MEM does not attempt to directly reconstruct the point sources but instead tries to prevent that this emission contaminates the rest of the components. Therefore, the point source contribution is just included in the formalism as an extra noise term. This is reflected in the second equality, where the instrumental noise and the point source emission has been combined in a general noise contribution.

As discussed in Hobson et al. (1998), MEM should not itself induce correlations between the elements of the reconstructed vector. However, the microwave components may well be correlated. In addition, if prior information is available we may wish to include it in the algorithm. In order to fulfill these requirements, the reconstruction is performed in terms of a vector of ‘hidden’ variables  $\mathbf{h}$ . The vector of physical variables  $\mathbf{s}$  is subsequently found as

$$\mathbf{s} = \mathbf{L}\mathbf{h}, \quad (3)$$

$$\mathbf{C} = \mathbf{L}\mathbf{L}^T, \quad (4)$$

$$\mathbf{C} = \langle \mathbf{s}(k)\mathbf{s}^\dagger(k) \rangle \quad (5)$$

where the dagger denotes the Hermitian conjugate.  $\mathbf{C}$  is the signal covariance matrix, which contains at the  $p$ -th diagonal element, the value of the power spectrum of the  $p$ -th physical component at the reference frequency  $\nu_0$ , whereas the off-diagonal elements contain the cross-power spectrum between the different components.  $\mathbf{L}$  is a  $n_c \times n_c$  lower triangular matrix, obtained by performing a Cholesky decomposi-

tion of  $\mathbf{C}$ . Therefore, we can include in  $\mathbf{L}$  our prior knowledge, if available, of the power spectra and cross-power spectra of the microwave components. Note that  $\mathbf{L}$  itself can be iteratively determined by the MEM (Hobson et al. 1998). That is, a first reconstruction is obtained using an initial guess for  $\mathbf{L}$  and subsequently the power spectra of those reconstructions is estimated. These new power spectra are then used as a starting point for the next iteration and the process is repeated until convergence is achieved.

Following Bayes' theorem, we choose as the estimator  $\hat{\mathbf{h}}$  of the hidden vector to be the one that maximises the posterior probability given by

$$\Pr(\mathbf{h}|\mathbf{d}) \propto \Pr(\mathbf{d}|\mathbf{h}) \Pr(\mathbf{h}) \quad (6)$$

where  $\Pr(\mathbf{d}|\mathbf{h})$  is the likelihood of obtaining the data given a particular hidden vector and  $\Pr(\mathbf{h})$  is the prior probability that contains our expectations about the hidden vector before acquiring any data.

To construct the likelihood function, we assume that the 'generalised' noise contribution (containing instrumental noise and emission from point sources) is well described by a Gaussian distribution, which has been shown to work reasonably well (Hobson et al. 1999a). Therefore, the likelihood function is given by

$$\begin{aligned} \Pr(\mathbf{d}|\mathbf{h}) &\propto \exp(-\boldsymbol{\zeta}^\dagger \mathbf{N}^{-1} \boldsymbol{\zeta}) \\ &\propto \exp[-(\mathbf{d} - \mathbf{R}L\mathbf{h})^\dagger \mathbf{N}^{-1} (\mathbf{d} - \mathbf{R}L\mathbf{h})] \\ &\propto \exp[-\chi^2(\mathbf{h})] \end{aligned} \quad (7)$$

where in the second line we have used (2). The noise covariance matrix  $\mathbf{N}$  has  $n_f \times n_f$  elements and at each  $\mathbf{k}$ -mode is given by

$$\mathbf{N}(\mathbf{k}) = \langle \boldsymbol{\zeta}(\mathbf{k}) \boldsymbol{\zeta}^\dagger(\mathbf{k}) \rangle. \quad (8)$$

Therefore, at any given Fourier mode, the  $\nu$ th diagonal element of  $\mathbf{N}$  contains the power spectrum at that mode of the instrumental noise plus the point source contribution to the  $\nu$ th frequency channel. The off-diagonal terms account for the cross-power spectra between different channels. Note that if the noise is uncorrelated between channels, only the point sources contribute to the off-diagonal elements.

Regarding  $\Pr(\mathbf{h})$ , MEM assumes an entropic prior probability for the hidden vector  $\mathbf{h}$  of the form

$$\Pr(\mathbf{h}) \propto \exp[\alpha S(\mathbf{h}, \mathbf{m})] \quad (9)$$

where  $S(\mathbf{h}, \mathbf{m})$  is the cross entropy of the complex vectors  $\mathbf{h}$  and  $\mathbf{m}$ , where  $\mathbf{m}$  is a model vector to which  $\mathbf{h}$  defaults in absence of data.  $\alpha$  is a regularising parameter that can be fixed in a fully Bayesian manner. The expression for the cross entropy for complex images and the method for determining  $\alpha$  are discussed in Hobson et al. (1998).

Taking into account equations (7) and (9), maximising the posterior probability  $\Pr(\mathbf{d}|\mathbf{h})$  with respect to  $\mathbf{h}$  is equivalent to minimising the function

$$\Phi_{\text{MEM}}(\mathbf{h}) = \chi^2(\mathbf{h}) - \alpha S(\mathbf{h}, \mathbf{m}). \quad (10)$$

Therefore the MEM reconstruction at each Fourier mode is given by the vector of hidden variables  $\mathbf{h}$  that minimises the previous equation.

## 2.2 MEM+MHW joint analysis

As mentioned in the previous section, MEM does not directly attempt to reconstruct a catalogue of point sources at each frequency due to the fact that this emission can not be factorised in a spatial template and a frequency dependence. Instead, point sources are included as an extra noise term with the aim of preventing them from contaminating the reconstructions of the rest of the microwave components. This approach has shown to work reasonably well for point sources with low to intermediate fluxes, greatly reducing the contamination due to this emission in the reconstructed CMB and the other microwave components (Hobson et al. 1999a). However, this method does have some limitations. MEM does not succeed on removing the brightest point sources, which are present in the reconstructions although with significantly reduced amplitudes. This is not surprising, since point source emission is modelled as an additional Gaussian noise and the brightest point sources are not well characterised by such a model. In order to solve this problem, the MEM has been combined with the MHW (Vielva et al. 2001b).

The MHW technique has been developed for the extraction of point sources from microwave maps. The method was first introduced in Cayón et al. (2000) and then improved in Vielva et al. (2001a) by including the concept of optimal scale. The technique was then extended to deal with spherical data using the spherical Mexican hat wavelet in Vielva et al. (2003), which provide a predicted catalogue of point sources from all-sky full-resolution Planck data.

In this section we outline the basics of the MHW technique and how to combine it with the MEM (for a more detailed derivation see Vielva et al. 2001a,b). The two-dimensional MHW is given by

$$\psi(x) = \frac{1}{\sqrt{2\pi}} \left[ 2 - \left( \frac{x}{R} \right)^2 \right] e^{-\frac{x^2}{2R^2}}. \quad (11)$$

where  $R$  is the wavelet scale. By convolving the data with the MHW, we obtain the so-called wavelet coefficients. The main idea behind the MHW technique is that point sources are amplified in wavelet space and, therefore, they can be better detected. Wavelet coefficient maps can be obtained for each wavelet scale  $R$ . Let us assume that a point source of amplitude  $B$  has been convolved with a Gaussian beam of dispersion  $\sigma_a$ . The value of the wavelet coefficient for scale  $R$  at the position of the source is given by

$$\frac{w(R)}{R} = 2\sqrt{2\pi} \frac{B}{A} \frac{(R/\sigma_a)^2}{(1 + (R/\sigma_a)^2)^2}, \quad (12)$$

where  $A$  is the area occupied by the point source.

The variance of the wavelet coefficient map at scale  $R$  can be calculated as

$$\sigma_w^2(R) = 2\pi R^2 \int dk P(k) k |\hat{\psi}(Rk)|^2, \quad (13)$$

where  $P(k)$  is the power spectrum of the map to be analysed and  $\hat{\psi}$  corresponds to the Fourier transform of the MHW.

As already mentioned, point sources are amplified in wavelet space, i.e., the level of the point sources relative to the dispersion of the map is higher in wavelet space than in real space:

$$\frac{w(R)}{\sigma_w(R)} > \frac{(B/A)}{\sigma}, \quad (14)$$

where  $\sigma$  is the dispersion of the observed map (dispersion in real space). In order to obtain the best conditions to detect point sources, the first term in the previous equation should be as high as possible. To do this, the method looks for an optimal scale  $R_{\text{opt}}$  that maximises that quantity and therefore gives the maximum amplification of the point sources in wavelet space. Taking into account equations (12) and (13)  $R_{\text{opt}}$  can be easily obtained directly from the data, since the optimal scale only depends on  $\sigma_a$  and the power spectrum of the map to be analysed. As expected,  $R_{\text{opt}}$  takes values around  $\sigma_a$ , since this is the scale that characterises the point sources. The background of the image also plays a role in determining  $R_{\text{opt}}$ . Backgrounds with high power at scales larger than the beam size, will tend to move  $R_{\text{opt}}$  towards smaller scales than  $\sigma_a$  and vice-versa.

The procedure to detect point sources is as follows. First, the optimal scale is found and the map is filtered with the MHW of that scale. All pixels above a  $5\sigma_w(R_{\text{opt}})$  threshold are considered as point sources candidates. The data map is additionally filtered with another three adjacent scales. Those four wavelet coefficients maps are used to estimate the amplitude of the source by fitting the ‘experimental’  $w(R)$  curve at the position of the candidate to the expected theoretical values given by equation (12). If the fit is good, the candidates are accepted as point sources, if not, they are discarded.

The combination of the MEM and MHW consists on applying sequentially each of the methods. First of all, the MHW is applied to each of the frequency maps, which allows one to detect the brightest point sources. These sources are subtracted from the original data and MEM is then applied to these ‘cleaned’ maps, modelling the unsubtracted point sources as an additional noise term. Since the MHW can successfully remove the brightest sources and MEM can deal with those with low to intermediate flux, both methods complement each other and the reconstructions of the different microwave components are significantly improved when combined. Moreover, an improved point sources catalogue at each frequency map can also be obtained with the following procedure. The reconstructed maps are used to generate ‘mock’ data which are subtracted from the original ones. This provides residual maps at each frequency channel which contain mainly contributions from point sources and instrumental noise plus some residuals from other emissions. The MHW is then applied to these residual maps to produce a point source catalogue at each frequency that reaches lower fluxes and errors than those obtained using only the MHW.

### 2.3 The Wiener filter

Wiener filter is defined as the linear filter that minimises the variance of the errors of the reconstruction (e.g. Rybicki & Press 1992). This technique was generalised to deal with multifrequency and multiresolution microwave data in Bouchet et al. (1996) and Tegmark & Efstathiou (1996). Hobson et al. (1998) derived the Wiener filter in a Bayesian context and compare its performance with MEM when reconstructing the microwave sky from simulated Planck observations, showing that MEM outperformed WF.

Following Hobson et al. (1998) we will derive the Wiener filter within the Bayesian framework. In this context, the solution of the Wiener filter is found by assum-

ing that the probability distribution of the sky emission is well described by a multivariate Gaussian characterised by a given covariance matrix. Therefore, the probability distribution of the vector  $\mathbf{s}$  at each Fourier mode is also described by a multivariate Gaussian distribution of dimension  $n_c$ . This leads to a prior probability of the form

$$\Pr(\mathbf{h}) \propto \exp(-\mathbf{s}^\dagger \mathbf{C} \mathbf{s}) \quad (15)$$

where  $\mathbf{C}$  is the signal covariance matrix defined in (5). Taking into account the form of the likelihood found previously (equation 7), the posterior probability is given by

$$\Pr(\mathbf{s}|\mathbf{d}) \propto \exp[-\chi^2(\mathbf{s}) - \mathbf{s}^\dagger \mathbf{C} \mathbf{s}] \quad (16)$$

or, equivalently,

$$\Pr(\mathbf{s}|\mathbf{d}) \propto \exp[-\chi^2(\mathbf{h}) - \mathbf{h}^\dagger \mathbf{h}] \quad (17)$$

where we have made use of equations (3-4). Therefore, the Wiener reconstruction at each Fourier mode can be found by minimising, with respect to the hidden vector  $\mathbf{h}$ , the function

$$\Phi_{\text{WF}}(\mathbf{h}) = \chi^2(\mathbf{h}) + \mathbf{h}^\dagger \mathbf{h} \quad (18)$$

and then obtain the physical components as  $\mathbf{s} = \mathbf{L}\mathbf{h}$ .

We would like to point out that Hobson et al. (1998) showed that WF can be seen as an approximation to MEM in the small fluctuation limit and, therefore, for Gaussian signals, both reconstructions become very similar.

### 2.4 Linear combination of frequency channels

If we assume that the foreground contamination is small in comparison with the CMB signal, a simple approach that combines linearly the different frequency channels (LCFC) in order to increase the signal-to-noise ratio can be used. In this case, the estimation of the cosmological signal in the sky at position  $\mathbf{x}$  is given by

$$\hat{s}_{\text{CMB}}(\mathbf{x}) = \sum_{j=1}^{N_m} w_j(\mathbf{x}) d_j(\mathbf{x}) \quad (19)$$

where  $N_m$  is the number of frequency maps to be combined (we do not necessarily include all the available frequency channels) and the data  $d_j$  are given in thermodynamic temperature. In order to reduce the effect of instrumental noise, the weights of the map are chosen to be inversely proportional to the noise variance at each position of the sky and therefore the coefficients  $w_j(\mathbf{x})$  are given by:

$$w_j(\mathbf{x}) = \frac{1}{\sigma_j^2(\mathbf{x})} \left[ \sum \frac{1}{\sigma_j^2(\mathbf{x})} \right]^{-1} \quad (20)$$

where  $\sigma_j^2(\mathbf{x})$  is the noise dispersion of the frequency map  $j$  at position  $\mathbf{x}$ . Note that this procedure provides a map with increased signal-to-noise ratio and well-known noise properties but it does not attempt to remove any foreground contamination. However, when dealing with real data, some subtraction of foregrounds will also be performed in the combined map. For instance the WMAP team has used this type of combination to produce a map on which performing Gaussianity studies (Bennett et al. 2003b; Komatsu et al. 2003) but, before combining the maps, a fit to Galactic templates was removed from each of them in order to remove foreground contamination. In particular, they use all the receivers at Q, V and W bands (at 41, 61 and 94 GHz), since

they are dominated, outside the Galactic plane, by the cosmological signal. On the contrary, they avoid to include in the combination the K and Ka bands (at 23 and 33 GHz) which contain significant Galactic emission.

For the sake of simplicity, we will mimic the procedure of template fitting by reducing the Galactic foregrounds present in each frequency channel, prior to the linear combination, down to a 10 per cent of its total amplitude. Therefore, when referring to the LCFC method, unless it is otherwise stated, we will assume that this foreground removal step has been previously performed.

### 3 THE GAUSSIANITY TEST

Given the importance of analysing the temperature distribution of the CMB fluctuations, many methods have been developed to perform Gaussianity studies. These include, among others, the Minkowski functionals (Coles 1998; Gott et al. 1990; Kogut et al. 1996; Komatsu et al. 2003), the bispectrum (Ferreira, Magueijo & Górski 1998; Heavens 1998; Magueijo 2000), properties of hot and cold spots (Coles & Barrow 1987; Martínez-González et al. 2000), geometrical estimators (Barreiro et al. 2001; Doré et al. 2003; Monteserín et al. 2005), extrema correlation function (Naselsky & Novikov 1995; Kogut et al. 1996; Barreiro et al. 1998; Heavens & Sheth 1999) goodness of fit tests (Cayón et al. 2003a; Aliaga et al. 2003, 2005), multifractals (Pompilio et al. 1995), partition function (Diego et al. 1999; Martínez-González et al. 2000), phase analysis (Chiang et al. 2003; Chiang, Naselsky & Coles 2004; Coles et al. 2004) and higher criticism statistic (Cayón et al. 2005).

In addition, wavelet techniques have been introduced in the last years for CMB analyses for both small patches of the sky and spherical data. Ferreira, Magueijo & Silk (1997) investigate a set of statistics based on cumulants and defined in wavelet space. Hobson, Jones & Lasenby (1999b) study the power of the cumulants of the distribution of wavelet coefficients at each scale to detect cosmic strings on small patches of the sky. This work was extended by Barreiro & Hobson (2001) who compare the performance of different algorithms to construct 2-dimensional wavelets. Forni & Aghanim (1999) proposed a similar method that was tested on simulated CMB maps containing secondary anisotropies (Aghanim & Forni 1999) and on the COBE-DMR data (Aghanim, Forni & Bouchet 2001). The skewness, kurtosis and scale-scale correlation coefficients of the COBE-DMR data in the QuadCube pixelization using planar orthogonal wavelets was carried out by Pando, Valls-Gabaud & Fang (1998). This analysis was extended by Mukherjee, Hobson & Lasenby (2000). Recently, wavelet methods have been adapted to deal with spherical data. Barreiro et al. (2000) and Cayón et al. (2001) studied the skewness, kurtosis and scale-scale correlation of the COBE-DMR data in HEALPix pixelization using the Spherical Haar Wavelet and the Spherical Mexican Hat Wavelet (SMHW), respectively. Martínez-González et al. (2002) compared the performance of these two spherical wavelets to detect non-Gaussianity. Cayón et al. (2003b) put constraints on the  $f_{NL}$  parameter from the COBE-DMR data using the SMHW. An analysis based also on the SMHW

has been performed on the WMAP data by Vielva et al. (2004) finding a non-Gaussian signature at scales of  $\sim 10^\circ$ . This work has been extended by Mukherjee & Wang (2004), Cruz et al. (2005) and McEwen et al. (2005). Finally, steerable wavelets on the sphere have been recently proposed by Wiaux, Jacques & Vanderghynst (2005a,b) to perform Gaussianity analysis of the CMB. A comparison of the performance of wavelet methods with other techniques can also be seen in Aghanim et al. (2003) and Cabella et al. (2004).

In the present work, we will use a wavelet-based method to detect non-Gaussianity following the ideas of Hobson et al. (1999b) and Barreiro & Hobson (2001). In this section we outline the basics of the method. For a more detailed description of the method, see the previous works. The wavelet transform has been extensively described elsewhere (e.g. Daubechies 1992). For instance, Burrus, Gopinath & Guo (1998) give a detailed introduction to wavelets. The basic idea behind the wavelet transform is to decompose the considered signal in a series of wavelet coefficients that keep simultaneous information of real and Fourier space. Therefore each coefficient can be associated to a position  $l$  and scale  $j$  of the image, what makes this analysis very useful in many applications. In general the position and scale parameters can take continuous values. However, for pixelized images is more convenient to restrict these parameters to take a set of discrete values. In particular, one can construct a discrete set of wavelets that act as a complete basis for the digitised image.

In 1-dimension, the wavelet basis is constructed from dilations and translations of the mother (or analysing) wavelet function  $\psi$  and a second related function called the father (or scaling) wavelet function  $\phi$ :

$$\begin{aligned} \psi_{j,l} &= 2^{\frac{j-J}{2}} \psi(2^{j-J}x - l), \\ \phi_{j,l} &= 2^{\frac{j-J}{2}} \phi(2^{j-J}x - l), \end{aligned} \quad (21)$$

where  $2^J$  is the number of pixels of the considered discrete signal  $s(x_i)$  and  $0 \geq j \geq J-1$  and  $0 \geq l \geq 2^J-1$  denote the dilation and translation indices, respectively.

There is not a unique choice for the wavelet basis. For this work, we will use the so-called Daubechies-4 wavelets that form a real, orthogonal and compactly supported wavelet basis (see Daubechies 1992 for the derivation of these functions). The discrete signal  $s$  at pixel  $x_i$  can then be written

$$s(x_i) = a_{0,0} \phi_{0,0}(x_i) + \sum_j \sum_l d_{j,l} \psi_{j,l}(x_i), \quad (22)$$

$a$ ,  $d$  correspond to the approximation and detail wavelet coefficients respectively. These coefficients can be obtained in a recursive way starting from the data vector  $f(x_l) \equiv a_{J,l}$ ,  $l = 0, \dots, 2^J - 1$

$$\begin{aligned} a_{j-1,l} &= \sum_m h(m-2l) a_{j,m} \\ d_{j-1,l} &= \sum_m g(m-2l) a_{j,m}. \end{aligned} \quad (23)$$

where  $h$ ,  $g$  are the low and high-pass filters associated to the scaling and analysing wavelet functions through the refinement equation (see e.g. Burrus et al. 1998).

At each iteration, the vector of length  $2^j$  is split into

two components:  $2^{j-1}$  detail coefficients and the same number of approximation coefficients. These approximation coefficients are then used as input for the next iteration to construct the detail and approximation components at the next larger scale. The process is repeated down to the lowest resolution level considered. This leads to a number of wavelet coefficients equal to the original number of pixels. As the index  $j$  decreases from  $J - 1$  to 0, the wavelet coefficients give information about the structure of the function on increasingly larger scales, with each scale a factor of 2 larger than the previous one.

The extension of the discrete wavelet transform to two-dimensions is not unique. Following Mallat (1989) we will construct two-dimensional bases as tensor products of the scaling and/or analysing wavelet at each scale  $j$ :

$$\begin{aligned}\phi_{j;l_1,l_2}(x,y) &= \phi_{j,l_1}(x)\phi_{j,l_2}(y) \\ \psi_{j;l_1,l_2}^H(x,y) &= \psi_{j,l_1}(x)\phi_{j,l_2}(y) \\ \psi_{j;l_1,l_2}^V(x,y) &= \phi_{j,l_1}(x)\psi_{j,l_2}(y) \\ \psi_{j;l_1,l_2}^D(x,y) &= \psi_{j,l_1}(x)\psi_{j,l_2}(y).\end{aligned}$$

where H, V and D stand for horizontal, vertical and diagonal. The wavelet basis constructed in this way is non-redundant and orthogonal.

Let us assume that we have an image with  $2^J \times 2^J$  pixels. With this scheme, the image (scale  $J$ ) is decomposed into an approximation and three detail (horizontal, vertical and diagonal) images corresponding to scale  $J - 1$ , with each of the images containing  $2^{J-1} \times 2^{J-1}$ . Note that the approximation image is basically a smoothed version of the input map, whereas the detail coefficients keep the information of the difference between the original and smoothed images. The algorithm is then applied again to the approximation coefficients at scale  $J - 1$  to produce the approximation and detail coefficients at scale  $J - 2$  and so on. Note that the coefficients at scale  $j$  keep information of the structure of the image at scales approximately equal to the pixel size times  $\sim 2^{J-j}$ .

In order to test the Gaussianity of the CMB, the considered temperature map is wavelet transformed using Daubechies-4. A certain statistic is then calculated at each wavelet scale for each of the three types of wavelet coefficients. In particular, following Hobson et al. (1999b), we will consider the fourth order cumulant, that can be estimated as

$$\begin{aligned}\hat{\kappa}_4(j,T) &= \frac{N_j^2[(N_j + 1)\hat{\mu}_4 - 3(N_j - 1)\hat{\mu}_2^2]}{(N_j - 1)(N_j - 2)(N_j - 3)} \\ \hat{\mu}_r(j,T) &= \langle (d_j^T - \langle d_j^T \rangle)^r \rangle.\end{aligned}\quad (24)$$

where  $\hat{\kappa}_4(j,T)$  corresponds to the fourth cumulant estimated at scale  $j$  for the  $T$  type of detail coefficient,  $d_j^T$  are the detail wavelet coefficients,  $N_j$  is the number of considered coefficients at scale  $j$  and  $\hat{\mu}_r(j,T)$  are the estimated central moments. The same procedure is repeated for a large number of Gaussian realisations (5000) with the same power spectrum as the test map. The  $\hat{\kappa}_4$  value obtained for the input map is then compared with the distribution of  $\hat{\kappa}_4$  obtained from the Gaussian realisations. Departures from this distribution will indicate a detection of non-Gaussianity. To avoid spurious boundary effects we do not include in the analysis those coefficients that contain information from pixels close to the

Frequency (GHz)	Fractional bandwidth	FWHM (arcmin)	Pixel size (arcmin)	$\sigma_{noise}$ ( $\times 10^{-6}$ )
30	0.2	33.0	6.0	2.0
44	0.2	24.0	6.0	2.7
70	0.2	14.0	3.0	4.7
100	0.33	9.2	3.0	2.0
143	0.33	7.1	1.5	2.2
217	0.33	5.0	1.5	4.8
353	0.33	5.0	1.5	14.7
545	0.33	5.0	1.5	147
857	0.33	5.0	1.5	6700

**Table 1.** Characteristics of the Planck satellite at the 9 frequency channels. The central frequency and fractional bandwidth are given in columns 1 and 2. The antenna full-width half-maximum (FWHM) is given in column 3 (a Gaussian pattern is assumed for all channels). The characteristic pixel sizes are shown in column 4. Finally, the fifth column gives the expected instrumental noise (assumed to be Gaussian) in  $\Delta T/T$  per resolution element (which is assumed to be a square pixel of size the corresponding FWHM).

borders (in particular, we do not consider ten rows/columns in each border).

## 4 THE SIMULATED DATA

In order to test the effect of component separation on the distribution of the CMB, we have generated simulated observations of small patches ( $12.8^\circ \times 12.8^\circ$ ) of the microwave sky according to the characteristics of the Planck satellite (see table 1). The simulations contain, in addition to the cosmological signal, Galactic foregrounds (thermal dust, free-free and synchrotron), thermal and kinematic Sunyaev-Zeldovich effects, extragalactic point sources and Gaussian white noise.

We have used two reference CMB maps for our simulations. On the one hand, we have generated a Gaussian CMB map assuming the standard  $\Lambda$ CDM model (whose power spectrum was generated using CMBFast, Seljak & Zaldarriaga 1996). On the other hand, since we would like to test the effect of component separation on intrinsic non-Gaussianity, we have also used a simulated CMB map of cosmic strings (Bouchet, Bennett & Stebbins 1988). Given that recent CMB experiments have ruled out pure topological defect based scenarios (e.g. Bouchet et al. 2001) we will construct CMB maps with different proportions of the Gaussian and cosmic strings maps. Fig. 1 shows the Gaussian CMB, the cosmic strings simulation and a map with a mixture of the two components.

As Galactic foregrounds we have included simulations of synchrotron, thermal dust and free-free emissions, which have been simulated at the frequency of 353 GHz. The different emissions have been simulated assuming that the frequency dependence is spatially constant. The synchrotron template at this frequency has been obtained using the model of Giardino et al. (2002). To simulate this component at the different Planck frequencies we have rescaled this template using a power law  $I_\nu \propto \nu^{-\alpha_{\text{syn}}}$  with  $\alpha_{\text{syn}} = -0.9$ . The thermal dust template has been generated using the model of Finkbeiner, Davis & Schlegel (1999). For simplicity, we have then assumed a simple grey body law with param-

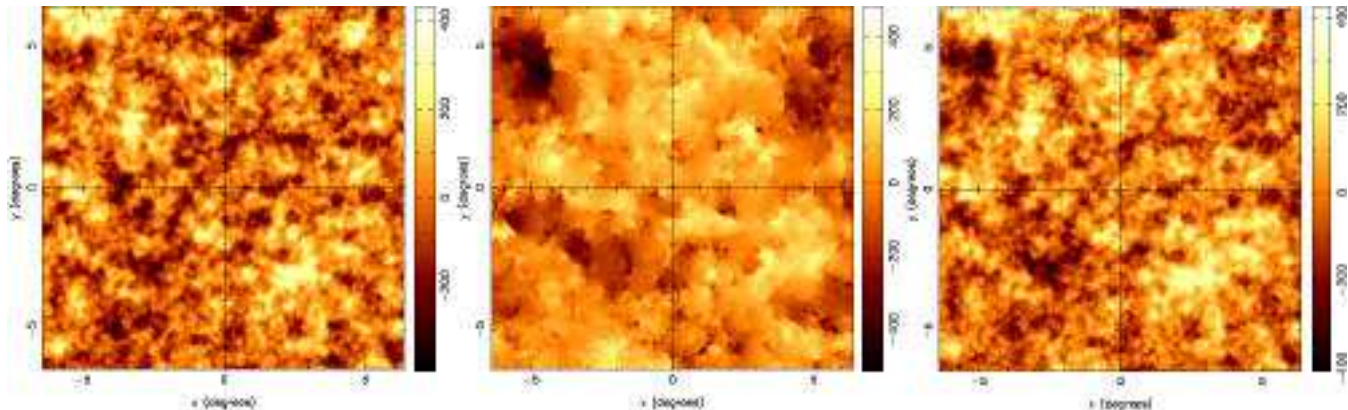


**Figure 1.** Test CMB maps used in the simulations. The different panels correspond to: Gaussian CMB (left), cosmic strings (middle), and Gaussian CMB plus cosmic strings in proportion 2:1 (right). The maps have been smoothed with a Gaussian beam of  $\text{fwhm}=5'$  and the units are thermodynamic temperature in  $\mu\text{K}$ .

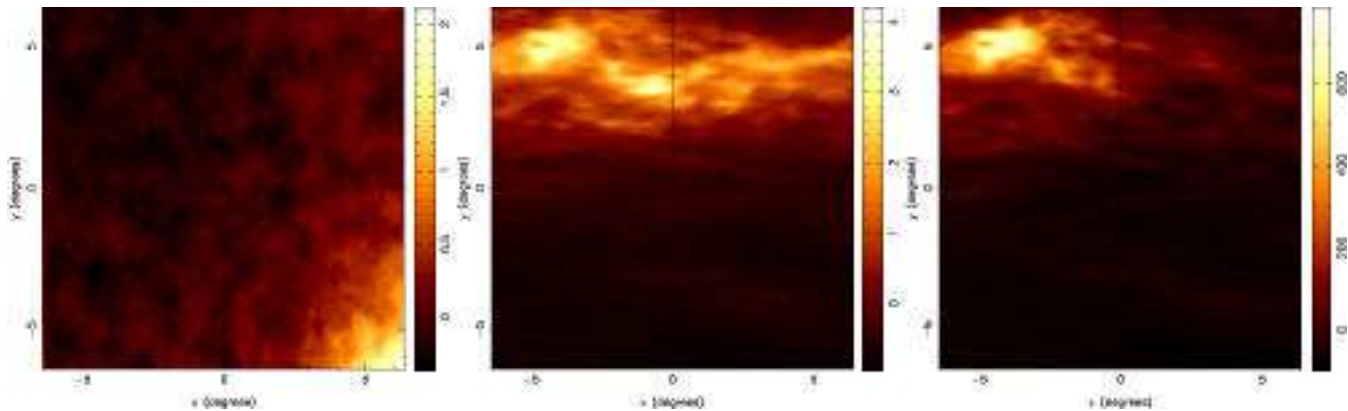


**Figure 2.** Simulated synchrotron (left), free-free (middle) and dust (right) emissions for our reference zone (region 3) at 300 GHz. The maps have been smoothed with a Gaussian beam of  $\text{fwhm}=5'$  and the units are thermodynamic temperature in  $\mu\text{K}$ .

ters  $T_d = 18\text{K}$  and  $\beta_{\text{emis}} = 2.0$  to simulate the contribution of this component at the Planck frequency maps. Finally, the free-free has been simulated using the correlation with dust emission in the way proposed by Bouchet & Gispert (1999). The template has then been extrapolated to the considered frequencies using a power law with  $\alpha_{\text{ff}} = -0.16$ . In order to test the robustness of the results we have tested the methods using four different Galactic regions of the sky with  $|b| > 20^\circ$ . The dispersion of the three Galactic components at the frequency of 300 GHz for the four considered regions is given in Table 2. Two of the regions (1 and 3) are within the brightest 2 per cent of the sky in dust emission, whereas the other two regions (2 and 4) correspond to more typical regions with lower Galactic dust emission. Fig. 2 shows the synchrotron, free-free and dust components for one of the considered regions of the sky.

The kinematic and thermal SZ effects have been simulated using the model of Diego et al. (2001) for the standard  $\Lambda\text{CDM}$  model. The radio and infrared point sources have been simulated according to the model of Toffolatti et al. (1998) (for recent improvements of this model, see de Zotti et al. 2005 and González-Nuevo, Toffolatti & Argüeso 2005) for the same cosmological model. Finally, we have simulated the in-

	Region 1	Region 2	Region 3	Region 4
Dust	292.9	50.33	115.8	26.7
FF	1.46	0.89	0.91	0.42
Synch.	1.29	0.09	0.28	0.70

**Table 2.** Dispersion of the three Galactic components for the four considered regions at 300 GHz smoothed with a Gaussian beam of 5 arcminutes. The units are thermodynamical temperature in  $\mu\text{K}$ .

strumental noise as Gaussian white noise according to the Planck characteristics.

Planck simulated data generated from the reference Gaussian CMB and the Galactic foregrounds of Fig. 2 (region 3) are given in Fig. 3. Table 3 gives the contribution in rms of each microwave component at each frequency channel for the same case.

## 5 RESULTS

We have performed our wavelet analysis on the recovered CMB maps obtained with the three considered reconstruction methods. We have also studied different input CMB

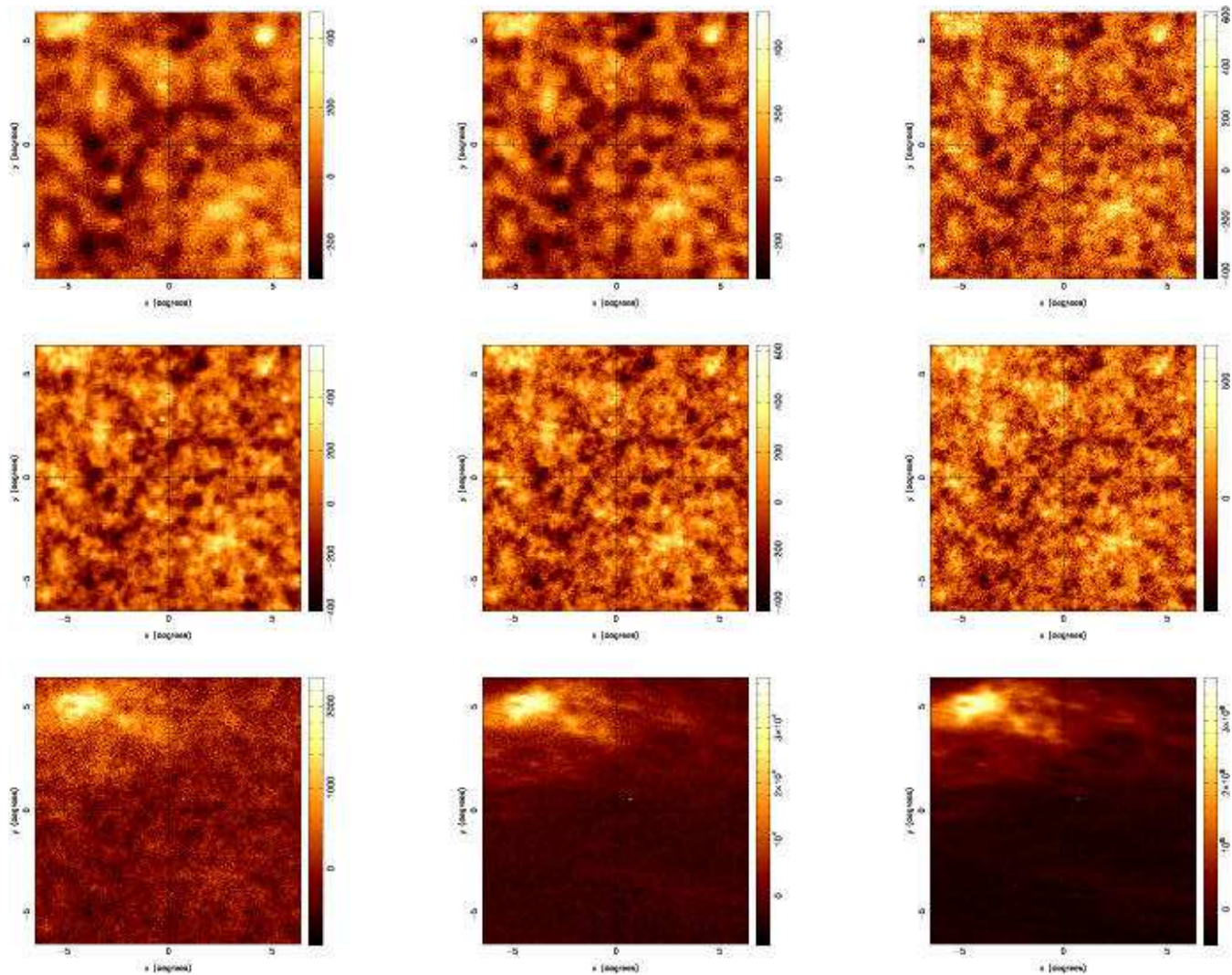


**Figure 3.** Simulated Planck data containing Gaussian CMB, Galactic synchrotron, dust and free-free emissions, thermal and kinematic Sunyaev-Zeldovich effects, extragalactic point source emission and white noise. From left to right and top to bottom the different panels correspond to 30, 44, 70, 100, 143, 217, 353, 545 and 857 GHz channels. The units are thermodynamic temperature in  $\mu\text{K}$ .

Frequency (GHz)	CMB	kSZ	tSZ	Dust	Free-free	Synchrotron	Point sources
30	72.8	0.29	2.15	0.25	18.6	29.6	19.9
44	83.3	0.37	2.70	0.54	8.48	10.3	13.1
70	97.7	0.53	3.55	1.45	3.40	2.98	9.31
100	105.7	0.67	3.78	3.35	1.80	1.23	7.75
143	109.8	0.79	2.95	8.35	1.08	0.57	5.38
217	113.4	0.95	0.00	31.5	0.80	0.31	5.10
353	113.4	0.95	7.17	284.8	1.18	0.32	17.1
545	113.4	0.95	17.4	5455.5	5.10	1.00	287.7
857	113.4	0.95	33.2	525918	130.4	18.4	13588

**Table 3.** Dispersion of the different microwave components in the Planck simulated data maps given in Fig. 3 (corresponding to region 3). The units are thermodynamical temperature in  $\mu\text{K}$ .

maps. First of all, we have produced Planck simulated data using our reference Gaussian CMB map and have studied if the reconstruction techniques preserve the Gaussian character of the temperature fluctuations (§5.1). Secondly, we have considered two different non-Gaussian CMB maps (containing different proportions of cosmic strings) and have studied

if the underlying non-Gaussianity is still detected in the reconstructed temperature map (§5.2). To understand better the effect of component separation techniques on the CMB we have neglected the effect of point sources in these two first cases, since this contaminant needs to be treated in a very different way. In a third case, we include the emission coming

from point sources in the Planck simulated data and study the effect of this contaminant when the underlying CMB map is Gaussian. The study is done on reconstructed maps obtained using MEM and the MEM+MHW joint analysis (§5.3).

In order to test the robustness of the results we have obtained the CMB reconstruction using simulated data of four different Galactic regions of the sky (see Table 2). We have found that the output of the Gaussian analysis is quite insensitive to the choice of the Galactic region and therefore we present our results only for simulations constructed using the Galactic templates of Fig. 2. We have also tested our results with different noise realisations, finding that the conclusions of the analysis are not modified.

For the LCFC, different combinations of frequency maps have been tried. In particular, we have found that the combination of the 143 and 217 GHz channels is the best choice for the considered cases in the sense of retaining the underlying CMB temperature distribution. Therefore, unless it is otherwise stated, we show our results for this particular combination.

### 5.1 Gaussian case

The CMB reconstructed maps obtained from the Planck simulated data for the input Gaussian CMB are given in Fig. 4. The different panels correspond to the reconstructions obtained using MEM (left), WF (middle) and the LCFC using the 143 and 217 GHz channels (right). These maps should be compared with the input Gaussian CMB of Fig. 1. Note that the MEM and WF reconstructed maps look very similar. The LCFC has a lower resolution than the MEM and WF reconstructions, since these two methods perform a (partial) deconvolution of the signal.

Fig. 5 shows the power spectra of the previous reconstructed CMB maps versus the input one. The solid line shows the power spectrum of the input Gaussian map, given in the left panel of Fig. 1. As shown in previous works, MEM (dash line) can recover reasonably well the CMB power spectrum up to  $\ell \lesssim 2000$ , whereas WF (dot-dash line) starts to underestimate the  $C_\ell$ 's around  $\ell \sim 1500$ . The dot line corresponds to the LCFC, where we appreciate two differences with respect to the input power spectrum: a defect of power at intermediate  $\ell$ 's, since the combined map has a lower resolution than the one of the input, and an excess at the higher multipoles, due to the presence of instrumental noise in the combined map. This curve can also be compared with the dash-three dots line, which corresponds to the power spectrum of a combined map obtained from data channels where only CMB is present. This represents the best reconstruction that could be achieved with the LCFC. We see that the reconstructed LCFC follows reasonably well this ideal LCFC power spectrum up to  $\ell \sim 1500$ .

In order to test the effect of the component separation technique on the underlying distribution of the CMB, we have applied our wavelet method to these three reconstructed CMB maps and compared the results with the input one. Figs. 6 and 7 show the value of  $\kappa_4$  (solid squares) at each wavelet scale for the input and reconstructed CMB maps. As already mentioned there are three different kinds of wavelet coefficients for the type of wavelet that we are using: vertical, horizontal and diagonal. Horizontal and ver-

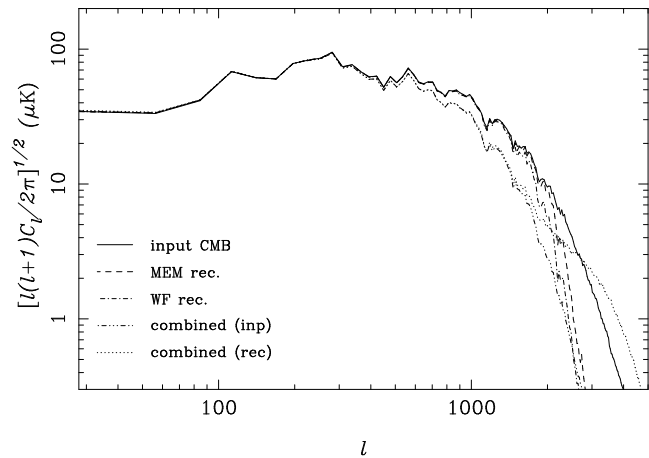


**Figure 5.** Power spectra obtained from the input and reconstructed CMB maps for the Gaussian case smoothed with a Gaussian beam of  $\text{fwhm}=5$  arcmin (see text for details).

tical details should be statistically equivalent, but we obtain different levels of detection because we are looking at a particular realisation. The  $x$ -axis on the plots gives the numbering  $k$  of the regions which goes as follows: region 1 corresponds to the approximation coefficients at the lowest resolution; regions 2,3,4 correspond to vertical, horizontal and diagonal details respectively for the largest scale ( $j = 1$ ); regions 5,6,7 give the three details in the same order for the next scale ( $j = 2$ ) and so on. The last scale ( $j = 26$ ) is not obtained from wavelet coefficients but corresponds to the value of  $\kappa_4$  obtained directly from the temperature map. Table 4 gives the correspondance between the region number  $k$  with the scale  $j$  and type of coefficients. It also gives an estimation of the scale corresponding to each wavelet region. Since no coefficients are retained at the lowest regions, the  $x$ -axis runs only from  $k = 8$  to 26. The open circle and error bars shown in the figures correspond to the average and the 68, 95 and 99 per cent acceptance regions obtained from 5000 Gaussian simulations with the same power spectrum as the test map. For comparison purposes the distributions of  $\kappa_4$  at each scale have been normalised to unit dispersion. Therefore the  $y$ -axis gives directly the values of  $\kappa_4$  in numbers of  $\sigma$  (note, however, that these distributions are not necessarily Gaussian and thus the number of  $\sigma$ 's in general will not correspond to the usual confidence intervals of the Gaussian case).

Fig. 6 gives the wavelet statistic for the input CMB map (top), the MEM (middle) and the WF (bottom) reconstructions. All maps have been smoothed with a Gaussian beam with  $\text{fwhm}=5'$  arcmin. As expected, the value of the  $\kappa_4$  statistics for the input (Gaussian) map lie within the error bars, i.e., the map is compatible with Gaussianity at all scales. We want to study if this behaviour is preserved in the reconstructed maps. We find that both MEM and WF produce very similar results and that the reconstructions are still compatible with Gaussianity. If we compare the results for the input and reconstructed maps, we find some small differences in the values of the wavelet statistics at large  $k$  (small scales), which are mainly due to an imperfect reconstruction because of the presence of instrumental noise. However, this effect is small and does not modify the con-

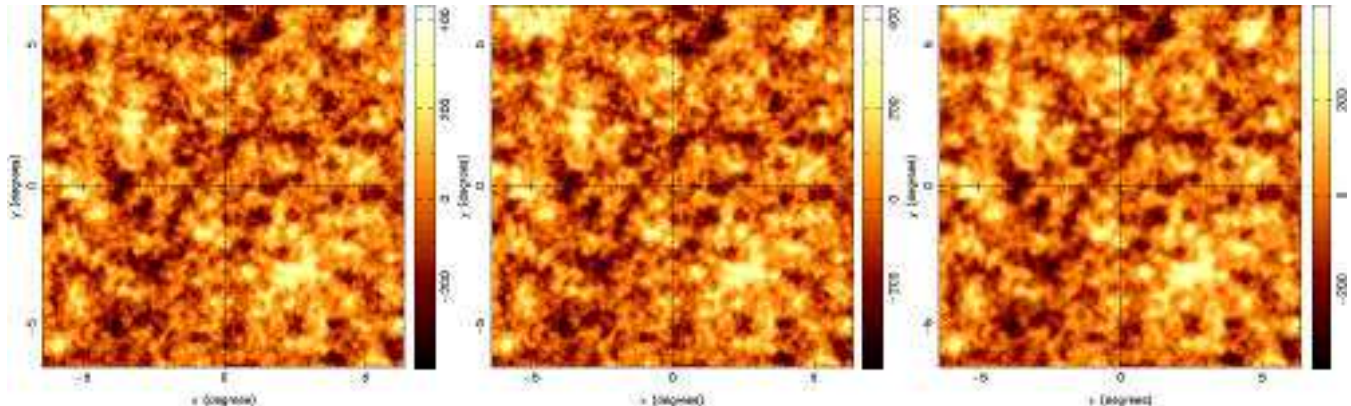


**Figure 4.** Reconstructed CMB map obtained with MEM (left), WF (middle) and a linear combination of the 143 and 217 GHz channels (right) from Planck simulated data using the Gaussian CMB as input. The maps have been smoothed with a Gaussian beam of  $\text{fwhm}=5$  arcmin and the units are thermodynamic temperature in  $\mu\text{K}$ .

**Table 4.** Correspondence of region number  $k$  with wavelet scale  $j$  and type of coefficient. A, V, H and D stand for approximation, vertical, horizontal and diagonal coefficients, respectively. The scale given in column 4 is calculated as  $1.5'(2^{J-j})$ , where  $2^J \times 2^J$  is the total number of pixels in the map. The total number of coefficients and those used in the analysis for each region are given in the fifth and sixth columns. The rest of the coefficients are discarded to avoid boundary effects.

region	$j$	detail	$\sim\text{scale}(')$	no.coeff.	used
1	1	A	$\geq 384$	4	0
2	1	V	384	4	0
3	1	H	384	4	0
4	1	D	384	4	0
5	2	V	192	16	0
6	2	H	192	16	0
7	2	D	192	16	0
8	3	V	96	64	16
9	3	H	96	64	16
10	3	D	96	64	16
11	4	V	48	256	144
12	4	H	48	256	144
13	4	D	48	256	144
14	5	V	24	1024	784
15	5	H	24	1024	784
16	5	D	24	1024	784
17	6	V	12	4096	3481
18	6	H	12	4096	3481
19	6	D	12	4096	3481
20	7	V	6	16384	14641
21	7	H	6	16384	14641
22	7	D	6	16384	14641
23	8	V	3	65536	60025
24	8	H	3	65536	60025
25	8	D	3	65536	60025

conclusion that the underlying CMB distribution is consistent with Gaussian, according to this test.

Fig. 7 shows the results obtained from the input (top) and reconstructed (bottom) combined maps, constructed by combining the 143 and 217 GHz channels. The input combined map is obtained as follows: first we create two maps containing only CMB, filtered with the corresponding beams of the 143 and 217 GHz channels; we then combine the two

maps weighting them accordingly to the noise levels of the two channels. This is the underlying CMB signal present in the reconstructed combined map and therefore we should use it for the comparison. Note that with this method, we can not aim to have better results than those obtained for the input combined map, since the reconstructed CMB signal is convolved and combined in that way. Finally, both maps have been smoothed with a Gaussian beam of  $\text{fwhm}=5$  arcmin in order to increase the signal to noise ratio of the reconstructed combined map. We find also in this case that the input and reconstructed maps are compatible with Gaussianity. There are again some small differences between both plots at high  $k$ 's which are mainly due to the presence of instrumental noise in the reconstruction.

Therefore, if the underlying CMB map is Gaussian, all the considered methods preserve the Gaussian character of the temperature distribution.

## 5.2 Non-Gaussian case

In order to test the effect of component separation on the underlying CMB temperature distribution, we have also considered two non-Gaussian test maps. In particular, we have considered mixtures of Gaussian CMB and cosmic strings in proportions 1:1 and 2:1 in rms. The proportion 2:1 corresponds approximately to the string contribution (18 per cent in the power spectrum) of the best fit to the CMB power spectrum using a mixture of inflation and cosmic strings found by Bouchet et al. (2001).

For the non-Gaussian case with proportion 1:1, we show in Fig. 8, the wavelet statistics for the 5 arcmin smoothed input (top), MEM (middle) and WF (bottom) maps. For the input map, we find very clear non-Gaussian detections for large  $k$ , greater than  $200\sigma$  at  $k=25$ . For the MEM reconstruction, the detections are also very clear (up to  $\sim 16.5\sigma$ ) but they have been significantly lowered with respect to the input map. Therefore there is a clear bias in the values of  $\kappa_4$ , and the CMB reconstruction tends to be more Gaussian than the input one. This is due to an imperfect reconstruction and loss of resolution caused mainly by the presence of instrumental noise. At those scales where the signal-to-noise ratio is low, the entropic prior tends to produce a conser-

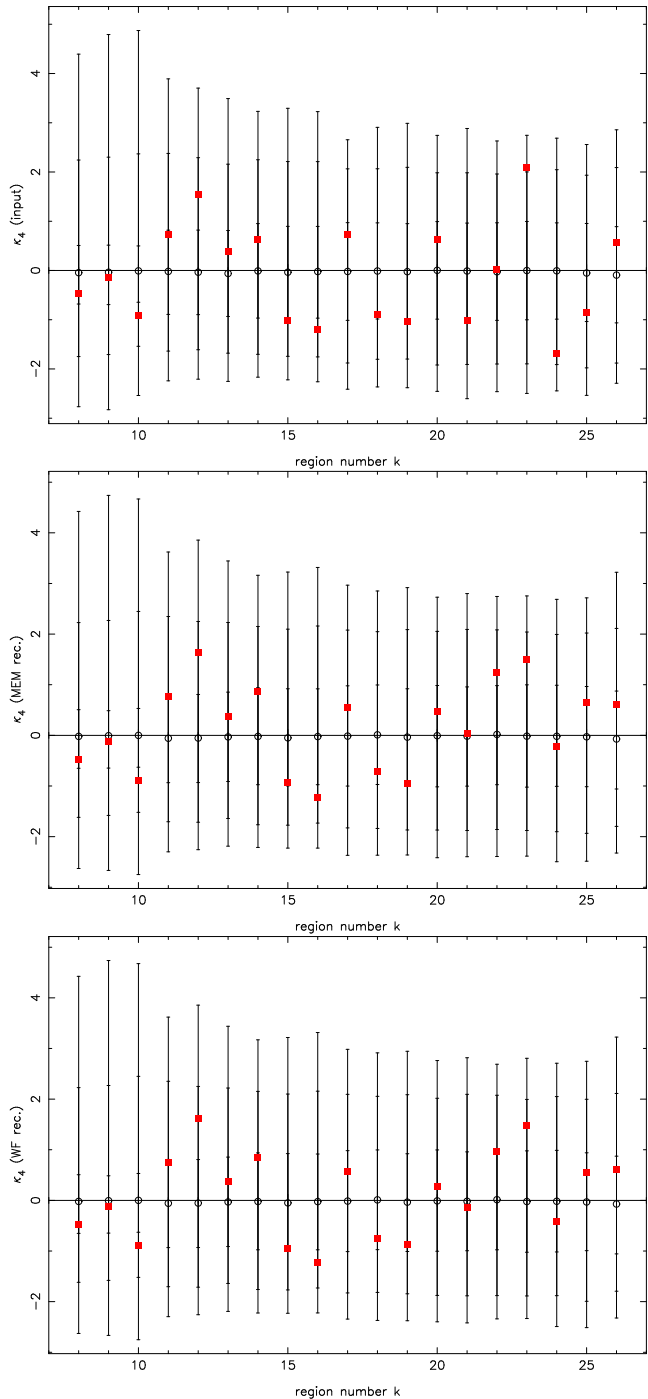


**Figure 6.** Value of  $\kappa_4$  versus region number  $k$  for the case of Gaussian CMB. The different panels correspond to the input CMB (top), MEM reconstruction (middle) and WF reconstruction (bottom). The open circles and the error bars correspond to the average and the 68, 95 and 99 per cent acceptance regions obtained from 5000 Gaussian simulations with the same power spectrum as the test map. The solid squares are the values obtained for the test map. Note that the small differences in the error bars (of the order of about a few percent) between the input and reconstructions are due to the limited number of simulations. In addition, since the reconstruction is not perfect, the power spectra of the reconstructed maps differ slightly from the input one, what also introduces small differences in the distribution of the  $\kappa_4$  values.

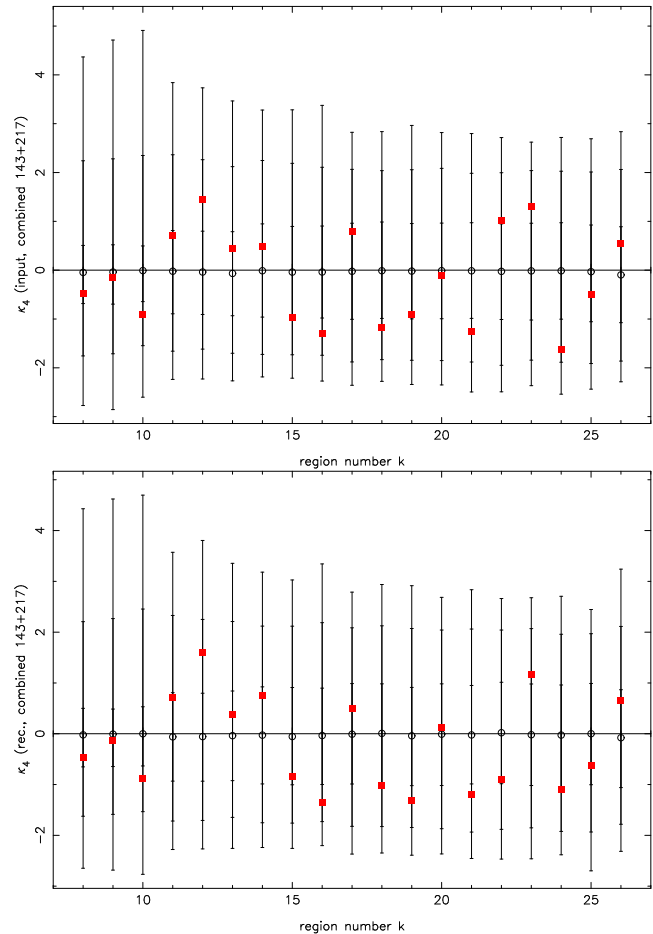


**Figure 7.** Value of  $\kappa_4$  versus region number  $k$  for the case of Gaussian CMB. The panels correspond to the input (top) and reconstructed (bottom) combined map using the 143 and 217 GHz channels

vative reconstruction with little structure, which causes the temperature distribution to be closer to Gaussian. A similar result is found for the WF reconstruction, where the highest non-Gaussian detection is at the level of  $\sim 15\sigma$ . Since WF assumes a Gaussian prior for the signal to be recovered, this tends to make the reconstruction even more Gaussian than does the entropic prior. Fig. 9 shows the results for the combined method. The non-Gaussianity is detected at the input combined map at a very high level ( $\lesssim 55\sigma$ ). In the reconstructed combined map, the non-Gaussianity is also clearly detected but at a lower level ( $\lesssim 12\sigma$ ). Therefore, the reconstructed map is also more Gaussian than the input one, mainly due to the contamination coming from instrumental noise. WF and MEM produce quite similar results, although, in general, the MEM reconstruction produces slightly higher detections than WF. Also, the level of the detections obtained with the LCFC are lower than those of the MEM and WF reconstructions. Using different noise realisations only produces a small dispersion in the detections and does not modify the results.

We have also considered map with a lower non-Gaussianity level constructed by mixing the Gaussian CMB map with the cosmic strings map in the proportion 2:1 in rms (right panel of Fig. 1). The reconstructions obtained us-

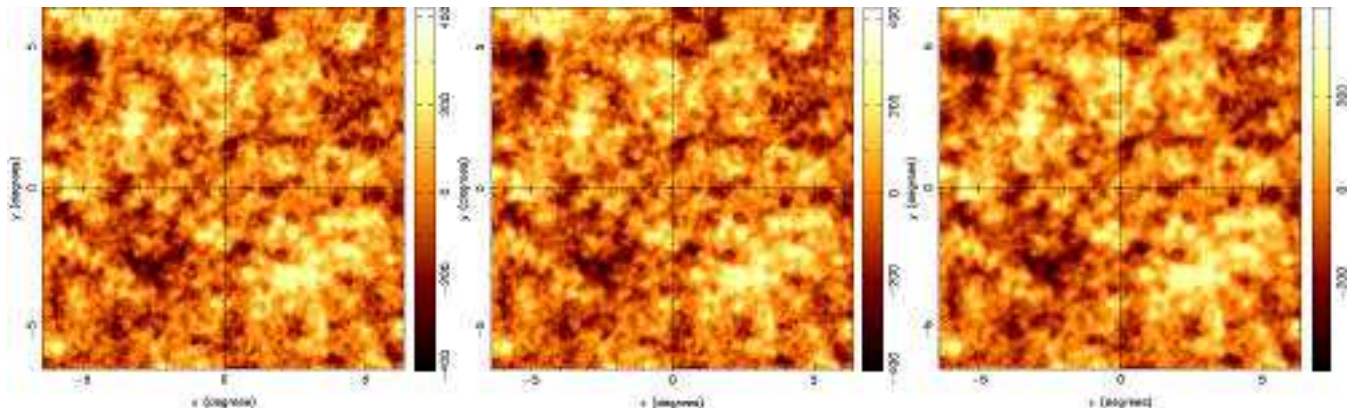


**Figure 10.** Reconstructed CMB map obtained with MEM (left), WF (middle) and a linear combination of the 143 and 217 GHz channels (right) from Planck simulated data using as input a mixture of Gaussian CMB and cosmic strings in proportion 2:1. The maps have been smoothed with a Gaussian beam of  $\text{fwhm}=5$  arcmin. The units are thermodynamic temperature in  $\mu\text{K}$ .

ing MEM, WF and the LCFC are given in Fig. 10 (smoothed with a Gaussian beam of  $\text{fwhm}=5$  arcmin). Note that again the MEM and WF reconstructions are quite similar, whereas the LCFC has lower resolution. The corresponding reconstructed and input power spectra are also given in Fig. 11. As before, MEM is able to recover the high  $\ell$ 's better than WF, whereas the LCFC presents an excess of power at high multipoles due to the presence of instrumental noise.

Fig. 12 shows the value of  $\kappa_4$  versus the region number for the input (top), MEM (middle) and WF (bottom) maps for this second non-Gaussian test map. The non-Gaussianity is still clearly detected in the input map although, as expected, the number and level of detections are lower than for the mixture in proportion 1:1. In particular there are 4 detections of non-Gaussianity outside the 99 per cent acceptance region, with the highest detection found at  $k = 25$  at the level of  $\sim 50\sigma$ . In the reconstructed maps, the level of the detections decrease dramatically. For MEM, we find 3 non-Gaussian detections at level  $\lesssim 3.5\sigma$ , whereas for WF there are the same 3 detections but at slightly lower level ( $\lesssim 3\sigma$ ). Therefore there is again a large bias in the sense of gaussianising the reconstruction. Since we are in the limit of the detection, different noise realisations can make that the detections fall inside the 99 per cent region of acceptance. In any case, we find again that the MEM reconstruction produces in general slightly higher detections than the one of WF.

With regard to the LCFC, the results are given in Fig. 13. Non-Gaussianity is detected at the  $\sim 8\sigma$  level in the input combined map. The reconstructed map shows a detection outside the 99 per cent acceptance region at region  $k = 23$ . However, this detection was present in the input only outside the 95 per cent acceptance region. This result is a combination of having a significant intrinsic  $\kappa_4$  value and the noise realisation and thus is not a robust detection. In fact, when using a different noise realisation, this detection disappears and other detections can appear. Therefore, we are again in the limit of detecting the non-Gaussianity. In any case, the levels of  $\kappa_4$  are lower than those in the MEM and WF reconstructions.

Thus, in all the considered cases, there is a clear bias for the three studied methods and the intrinsic non-Gaussianity is strongly reduced in the reconstructed map.

### 5.3 Effect of point sources

For simplicity, we have not included the emission of extragalactic point sources in the previous subsections. Now, we will include this contaminant in the simulations and study the reconstructions obtained using only MEM and the MEM+MHW joint analysis. We use the Gaussian CMB map given in the left panel of Fig. 1 as input.

Fig. 14 gives the reconstructions obtained using only MEM (top) and the MEM+MHW joint analysis (bottom) smoothed with a Gaussian beam of  $\text{fwhm}=5$  arcmin. The recovered power spectra for both cases is very similar to the one obtained for the MEM reconstruction of Fig. 5 (when point source emission was not included). However, even if not seen in the power spectrum, the MEM reconstruction is clearly contaminated by point source emission (see top panel of Fig. 14). This contamination is reduced when using the joint method (bottom panel of Fig. 14). This effect is also seen in Fig. 15, which shows the corresponding wavelet statistic for the previous reconstructed maps. These results should be compared with the top panel of Fig. 6, which shows the values of  $\kappa_4$  for the input CMB map. We find clear detections of non-Gaussianity in the MEM reconstructed map, at the level  $\lesssim 60\sigma$ . Since the underlying CMB signal is Gaussian, this is due to the presence of residual point source emission, which MEM has not been able to remove. However, when the MHW is used to subtract the brightest point sources prior to the application of MEM, this contamination is greatly reduced and the CMB reconstruction is again compatible with Gaussianity (bottom panel of Fig. 15). Similar results have been found when combining the MHW with WF or with the LCFC. If not subtraction of point sources is attempted, both methods detect residual point sources. In particular, for WF this detection is slightly lower than for MEM (since it tends to gaussianise more the residuals) whereas for the LCFC it is also reduced (due to the lower resolution of the combined map). But if the MHW is previously applied, the CMB reconstruction is also compatible with Gaussianity. Therefore, the removal of point source emission is crucial in order to avoid the introduction of spurious non-Gaussianity in the reconstructed CMB temperature distribution.

As a further test, we have also applied the MEM+MHW

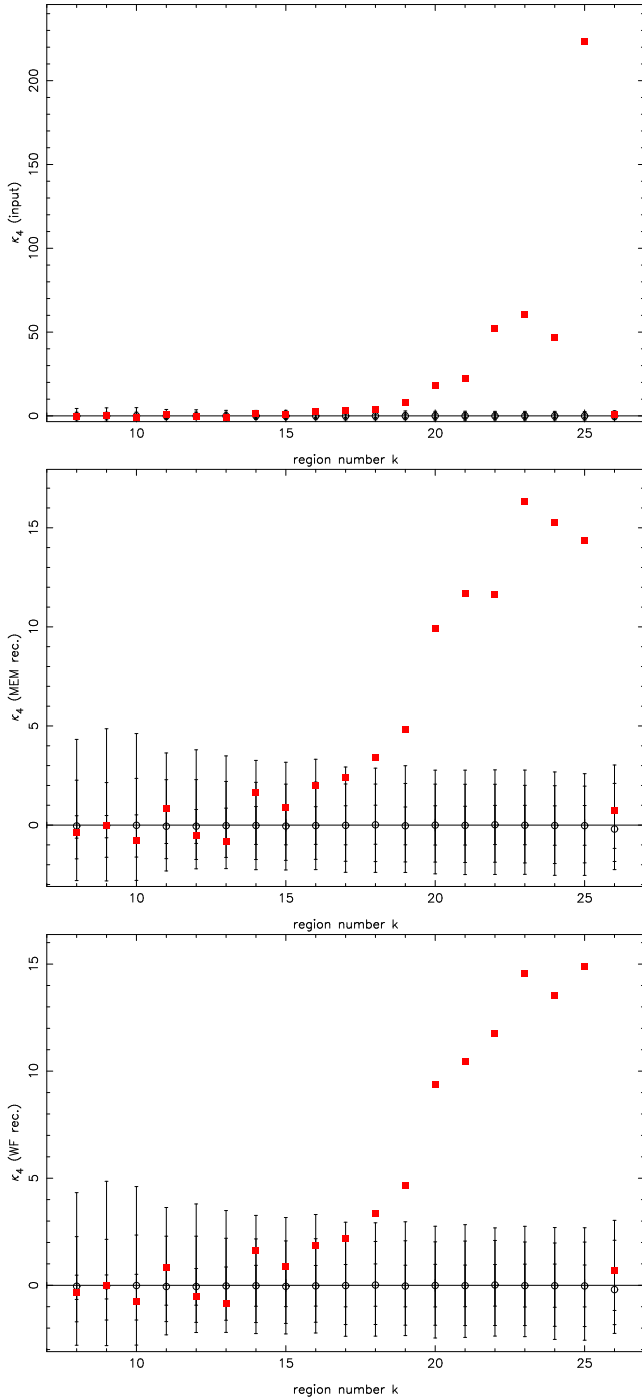


**Figure 8.** The value of  $\kappa_4$  versus the region number is shown for the case of a mixture of Gaussian CMB and cosmic strings in proportion 1:1. The plots correspond to the input CMB (top), MEM reconstruction (middle) and WF reconstruction (bottom).

joint analysis to Planck simulated data containing point sources and a non-Gaussian input CMB. In this case, we find that the level of the detection of non-Gaussianity is similar to that found in section 5.2 for the two considered proportions of cosmic strings.

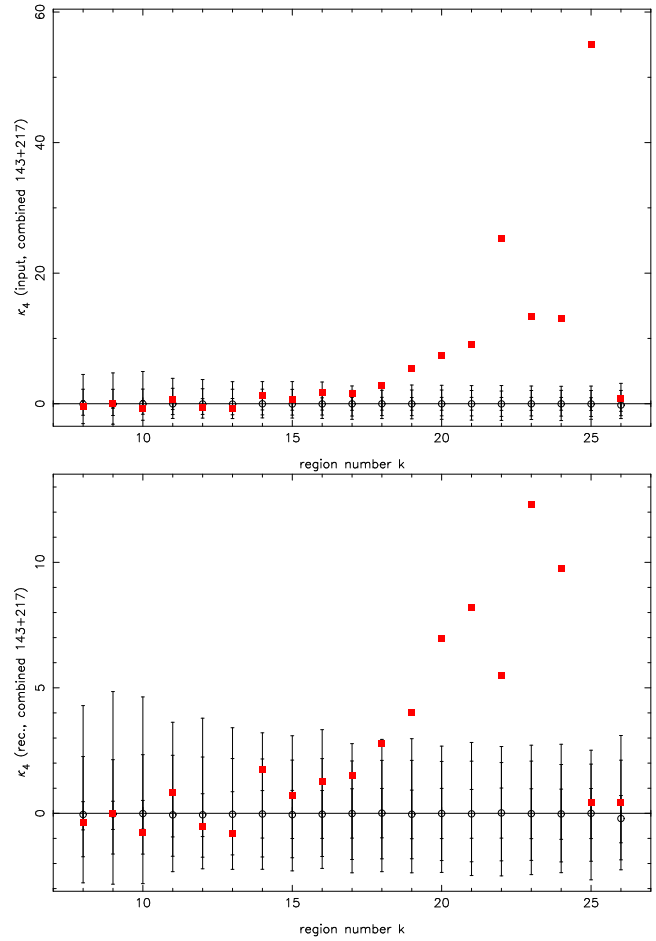


**Figure 9.** The value of  $\kappa_4$  for the input (top) and reconstructed (bottom) combined maps (143+217 GHz) for the case of a mixture of Gaussian CMB and cosmic strings in proportion 1:1.

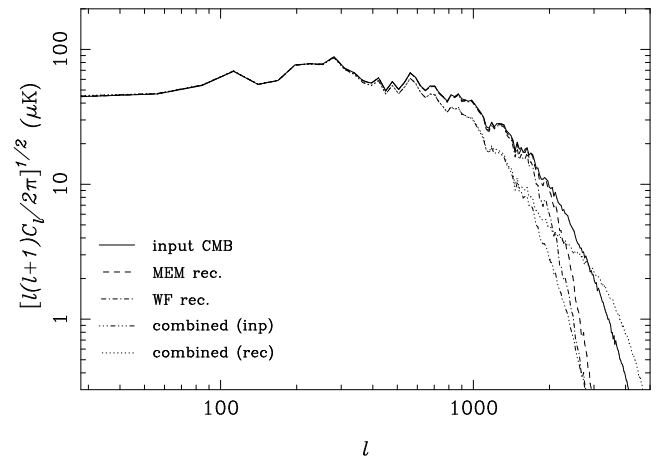


**Figure 11.** Power spectra obtained from the input and reconstructed CMB maps for the non-Gaussian case with a mixture of the Gaussian CMB and cosmic strings in proportion 2:1. The maps have been smoothed with a Gaussian beam of  $\text{fwhm}=5$  arcmin.

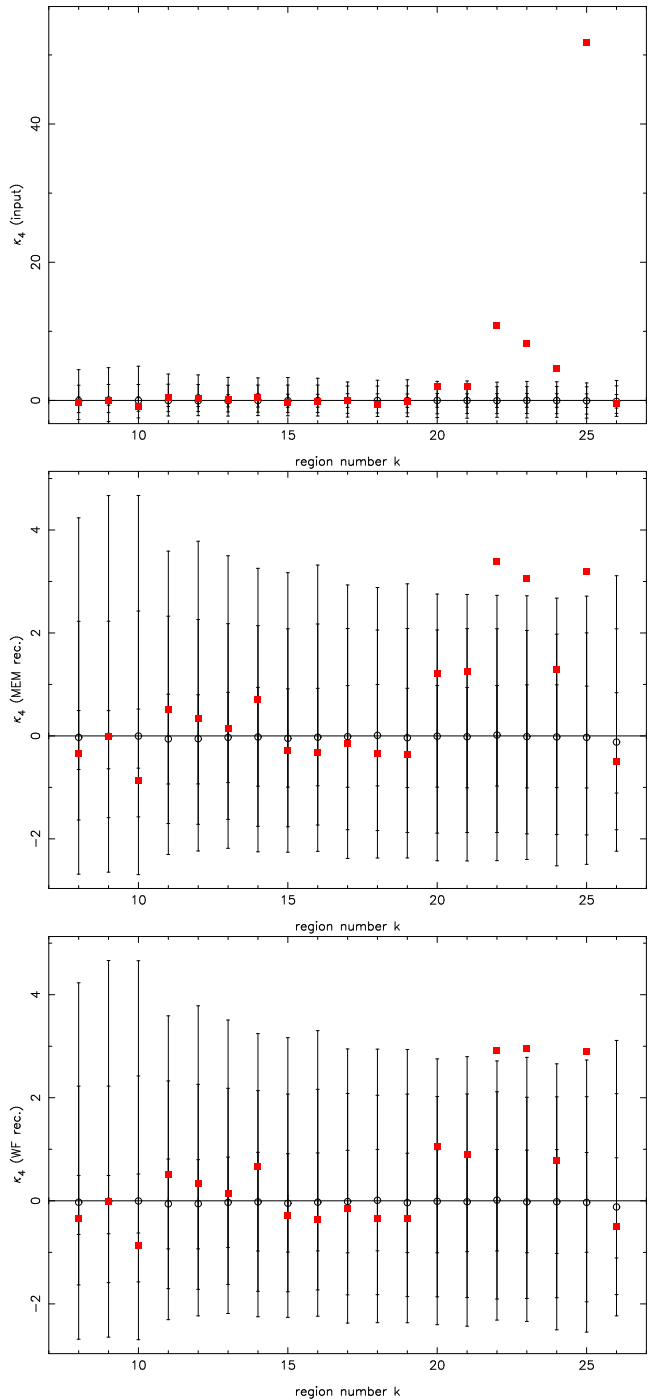


**Figure 12.** Values of  $\kappa_4$  at each wavelet region for the case of a mixture of Gaussian CMB and cosmic strings in proportion 2:1: input CMB (top), MEM reconstruction (middle) and WF reconstruction (bottom).

## 6 ROLE OF INSTRUMENTAL NOISE AND FOREGROUNDS

In order to test which is the effect of each of the elements that take part in the component separation method, we present in this section some additional tests. In particular, we perform first some analyses to understand the effect of the Galactic foregrounds and the SZ emissions, without in-

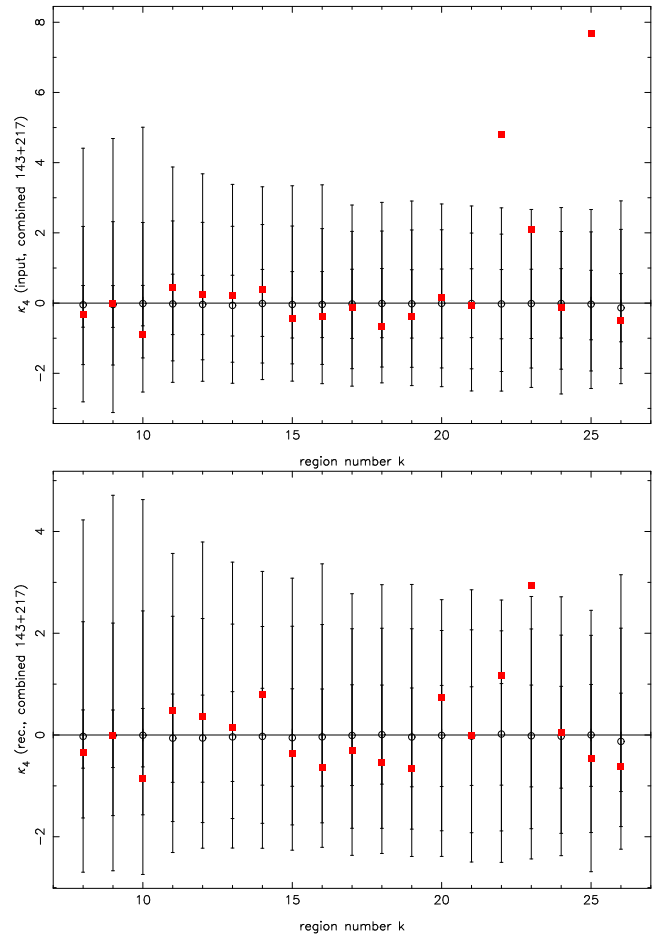


**Figure 13.** The values of  $\kappa_4$  versus the wavelet region are given for the input (top) and reconstructed (bottom) combined (143+217 GHz) maps corresponding to the case of a non-Gaussian initial CMB generated as the mixture of Gaussian CMB and cosmic strings in proportion 2:1.

cluding the contribution of point sources, on the CMB reconstructed distribution. Then, we consider the same case but reducing the level of noise by a factor of 10 and, finally, we further study the effect of including point sources.

### 6.1 Galactic foregrounds and SZ emission

First of all, we have applied our Gaussianity analysis to a low and a high frequency Planck channel (where the synchrotron and dust emissions are more important) without including point source emission in order to show how the wavelet coefficients are affected by the presence of foregrounds. Fig. 16 gives the values of  $\kappa_4$  for the 30 GHz (top) and 545 GHz (bottom) channels including the Galactic foregrounds of Fig. 2 as well as our reference Gaussian CMB and the thermal and kinetic SZ emissions (the results are qualitatively similar for the other three considered Galactic regions). Since the pixel size at 30 GHz is 6 arcmin, we consider wavelet regions only up to  $k = 19$ , whereas  $k = 20$  corresponds to the  $\kappa_4$  value of the real map. We see that, at this frequency, there are not deviations from Gaussianity in spite of having a certain contamination from synchrotron. At high Galactic latitude, this emission is subdominant in comparison with the CMB and

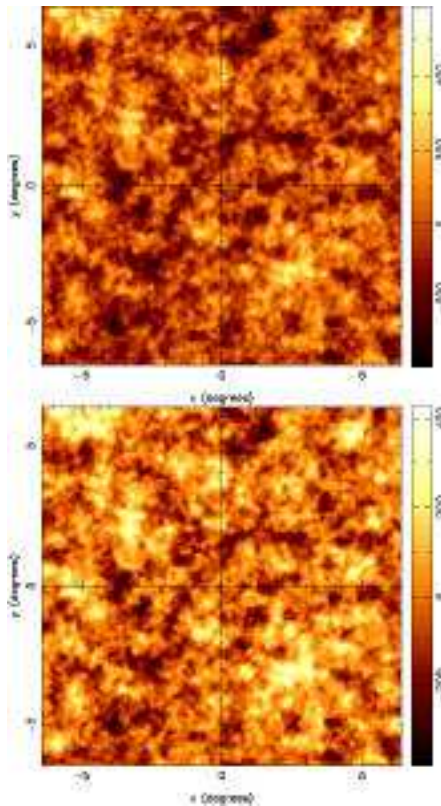


**Figure 14.** Reconstructed CMB map obtained with MEM (top) and MEM+MHW (bottom) for the case when point sources are included in the data. The reconstructions should be compared with the input Gaussian CMB (left panel of Fig. 1). The maps have been smoothed with a Gaussian beam of  $\text{fwhm}=5$  arcmin and the units are thermodynamic temperature in  $\mu\text{K}$ .

it is not seen in this test. We also have to point out that the most important contribution of the synchrotron is expected to occur at larger scales than those considered here, therefore the synchrotron could be important when analysing larger regions of the sky. Finally, one should bear in mind that the synchrotron template used in this work is based on the Haslam map, which has a resolution of  $0.85^\circ$  and therefore it does not contain real structure (only simulated) at the smallest scales, which may not be representative of the true emission. However, even with these uncertainties, we do not expect the results of this work to change with a more realistic simulation of synchrotron. This is so because the reconstructions obtained from MEM and WF were very robust under variations of the Galactic foregrounds and, with regard to the LCFC, the synchrotron is negligible at the considered frequency channels (143 and 217 GHz). Regarding the 545 GHz channel, which is completely dominated by dust emission, we see very clear non-Gaussian detections at different scales (bottom panel of Fig. 16). Non-Gaussian detections at different levels are also found at 353 GHz for the four considered Galactic regions whereas at 217 GHz there is one detection of non-Gaussianity only for the brightest region (region 1). Therefore, we see that the dust template is strongly non-Gaussian but for frequencies of 217 GHz or lower the dust emission seems to be, in general, already quite weak and should not affect our Gaussianity analysis (although,

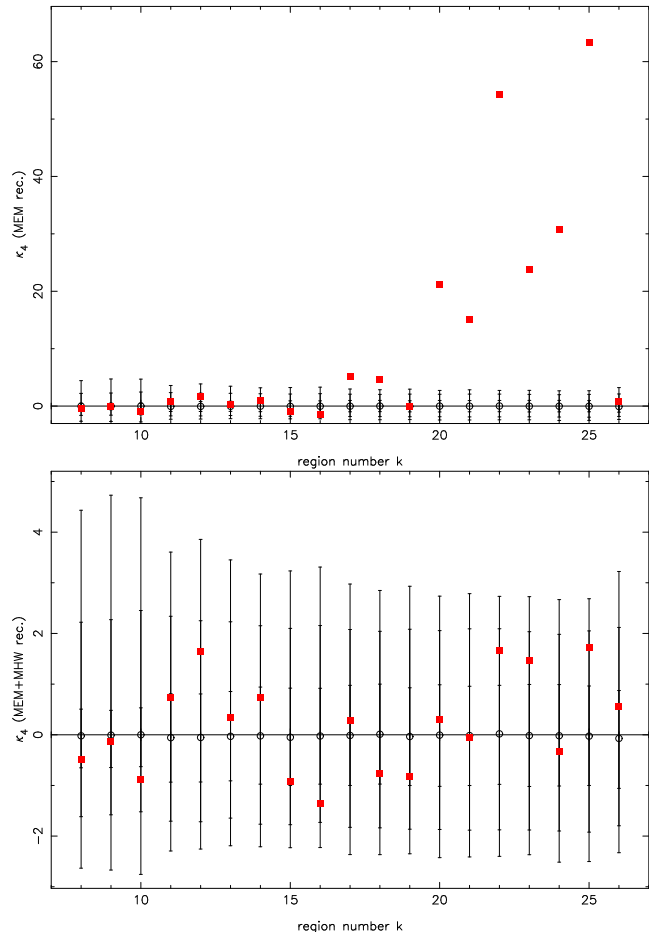


**Figure 15.** Values of  $\kappa_4$  for each wavelet region for the CMB reconstruction obtained using only MEM (top) and the MEM+MHW joint analysis (bottom) when point source emission is included in the data for an initial Gaussian CMB. The results should be compared with the top panel of Fig. 6, which shows the values of  $\kappa_4$  for the input CMB map.

of course, it could be more important at larger scales than those considered here). Of course, this is assuming that the uncertainties on the simulated dust emission are small.

To further test the effect of foregrounds we have repeated the analyses of sections 5.1 and 5.2 using data maps where the foreground components (Galactic emission and SZ) have been divided by a factor of 100. In this case the LCFC is done directly using these frequency maps (without further reducing the Galactic foregrounds). The results are very similar to those obtained in the previous section for both the Gaussian and non-Gaussian cases. These results confirm that, for the wavelet analysis presented in this work and within the uncertainties of our simulations, the Galactic foregrounds (for high Galactic latitude regions) and SZ emissions do not seem to introduce any spurious non-Gaussianity.

## 6.2 Instrumental noise

To understand the effect of instrumental noise on the CMB reconstructions, we have repeated the Gaussian analyses of sections 5.1 and 5.2 reducing the noise dispersion by a fac-

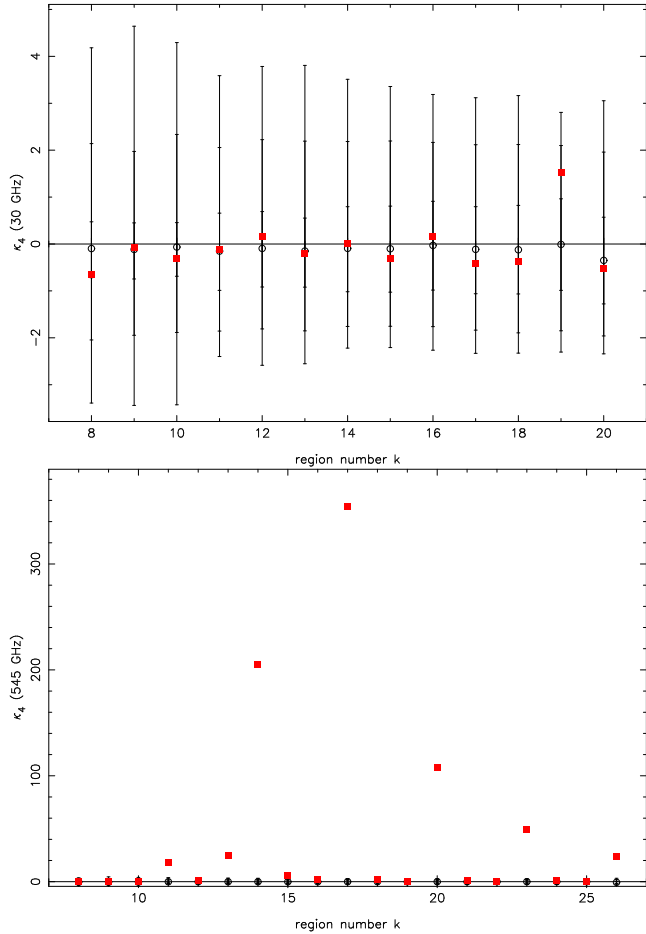


**Figure 16.** Values of  $\kappa_4$  for each wavelet region for the 30 GHz (top) and the 545 GHz (bottom) frequency channels simulated using the Galactic foregrounds given in Fig. 2. The 30 and 545 frequency channels have been smoothed with a Gaussian beam of 20 and 5 arcminutes respectively to reduce the instrumental noise. Note that since the 30 GHz channel has a pixel of 6 arcminutes, only wavelet regions with  $k \leq 19$  are considered, whereas  $k = 20$  corresponds in this plot to the value obtained from the real map.

tor of 10 (and again without including point sources). When the input CMB is Gaussian, the reconstructed CMB is again Gaussian for MEM, WF and LCFC. The main difference is that the values of  $\kappa_4$  of the reconstructed maps are closer to the same values in the input map. This is especially visible at the smallest scales (largest values of  $k$ ) which were more affected by the presence of noise. With regard to the non-Gaussian case, the detections are clearly improved for the three methods and for the two proportions of cosmic strings considered. Fig. 17 shows the  $\kappa_4$  statistics for the reconstructed CMB map using MEM (top), WF (middle) and the combined 143+217 GHz map (bottom) for a mixture of Gaussian CMB and strings in proportion 2:1. This figure should be compared with Fig. 12 and 13. It becomes apparent that lowering the noise allows a much better detection of the intrinsic non-Gaussianity in all the cases. Therefore, the instrumental noise is clearly impairing our ability to detect intrinsic non-Gaussianity. This also indicates that MEM and WF perform better than the simple LCFC not only because

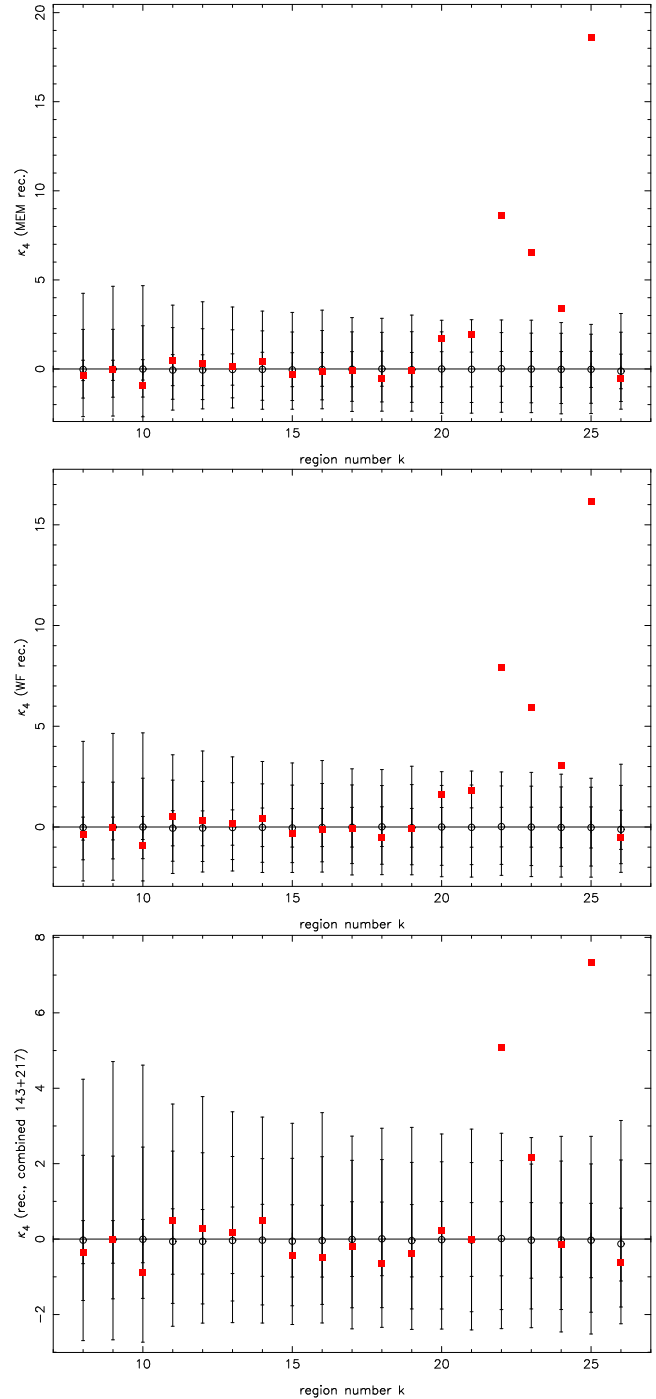


**Figure 17.** Values of  $\kappa_4$  at each wavelet region for the case of a mixture of Gaussian CMB and cosmic strings in proportion 2:1 where the noise has been reduced by a factor of 10. The different panels correspond to MEM reconstruction (top), WF reconstruction (middle) and 143+217 GHz combined map (bottom) smoothed with a Gaussian beam of  $\text{fwhm}=5$  arcminutes.

they remove better the foregrounds but mainly because they attempt to denoise (and deconvolve) the signal.

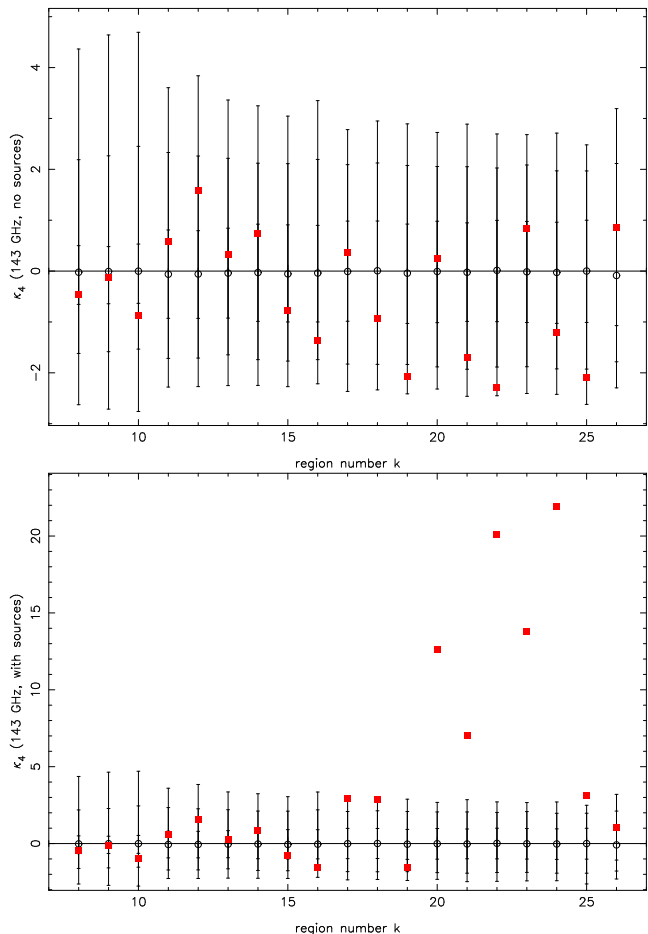


**Figure 18.** Values of  $\kappa_4$  at each wavelet region for the 143 GHz channel without including (top panel) and including the emission of point sources (bottom panel). In order to reduce the noise, both maps have been smoothed with a Gaussian beam with  $\text{fwhm}=5$  arcminutes.

### 6.3 Point sources

In section 5.3 we have showed that point sources can be a very damaging foreground and that is crucial to remove, at least, the brightest point sources in order to avoid the presence of spurious non-Gaussianity in the CMB distribution. As an example of the effect of extragalactic point sources, we show in Fig. 18 the  $\kappa_4$  statistics for the 143 GHz channel without including (top) and including (bottom) point source emission. It is clear that point sources are introducing important levels of non-Gaussianity in the data, especially at the smallest scales, even for the 143 GHz channel where the contribution of point sources is expected to be relatively small.

We would like to point out that we are performing our non-Gaussian analysis on a small patch of the sky of  $12.8^\circ \times 12.8^\circ$ . However Planck will provide all-sky observations of the CMB and therefore we expect to be able to analyse much larger regions of the sky. Since having a larger area of the sky will appreciably reduce the variance of the  $\kappa_4$  statistics we may wonder if, in this case, we would be able to detect the point source residuals even after subtracting the brightest point sources. We have tried to give an answer to this question with the following qualitative argu-

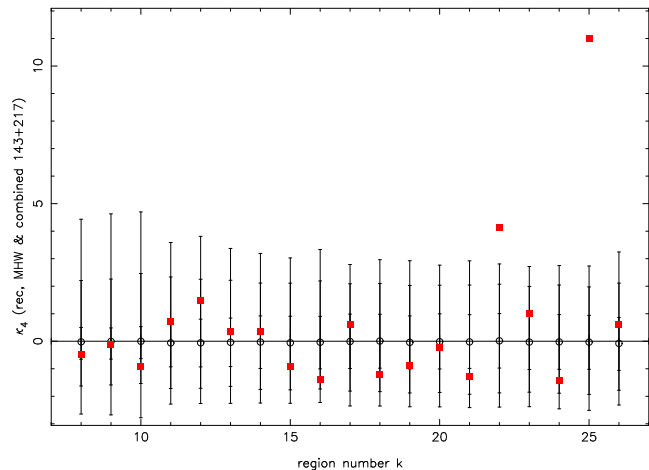


**Figure 19.** Values of  $\kappa_4$  at each wavelet region for the 143 and 217 GHz combined map including point source emission for a case where the instrumental noise has been reduced by a factor of 10. The combined map has been smoothed with a Gaussian beam with  $\text{fwhm}=5$  arcminutes. Before combining the maps, the brightest point sources have been removed using the Mexican Hat wavelet.

ment. For the LCFC, the part of the variance coming from Gaussian white noise will decrease as the considered area. For two-thirds of the sky this corresponds to a reduction in the part of the dispersion coming from the noise of the order of 10. Therefore, in order to mimic the case of performing the component separation in a larger area of the sky, we have constructed new data reducing the noise dispersion by a factor of 10 and subtracted from each channel the same catalogue of point sources as that of section 5.3. Then we have applied our non-Gaussianity test on the map obtained with the LCFC using the 143 and 217 GHz channel. The result is given in Fig. 19, showing a clear detection of non-Gaussianity. Of course, in the real case, the error bars will be further reduced, although not in such a straightforward way as for the white noise, since we are not considering the reduction of the variance corresponding to the CMB and the point sources themselves. But this means that our estimation can be considered as an upper limit to the error bars of the  $\kappa_4$  and thus the residual point source emission will be even more clearly detected.

For the case of MEM, given that is a non-linear process, the way in which the dispersion of the  $\kappa_4$  statistics scales with the area is not so simple, but we still expect our argument to hold qualitatively. We have performed the Gaussian analysis for the data with the noise level reduced by a factor of 10 using MEM+MHW and found again clear detections of non-Gaussianity due to the residual point sources.

Therefore, point source emission should be carefully reduced or masked on CMB data since otherwise it will introduce spurious non-Gaussianity on the analysed signal.

## 7 DISCUSSION

We have studied how different component separation techniques affect the underlying CMB temperature distribution. In particular, we have used Planck simulated data (including the cosmological signal, Galactic foregrounds, SZ effects

and instrumental noise) to reconstruct the CMB with MEM, WF and LCFC. We have also studied the effect that point source emission has in the reconstructed map obtained from MEM and a MEM+MHW joint analysis. The impact of the component separation method on the CMB has been quantified by performing a wavelet analysis of the reconstructed CMB map and compared it with the same analysis for the input map. Gaussian and non-Gaussian CMB simulations have been tested. We have also presented some additional tests to understand the effect of the different foregrounds and instrumental noise.

Using as input a Gaussian CMB map (and without including the emission from point sources in the data), the three considered methods lead to a CMB reconstructed map which is compatible with Gaussianity. Therefore, none of them introduces spurious non-Gaussianity in the underlying CMB temperature distribution. However, when the input CMB distribution is non-Gaussian, all the methods introduce a strong bias in the reconstructed map, which clearly reduces the level of the intrinsic non-Gaussian detections when compared with the input map. As has been shown in section 6.2, this effect is mainly due to the presence of instrumental noise which leads to an imperfect reconstruction.

WF assumes a Gaussian prior for the signal to be reconstructed and therefore it is expected to perform well when the underlying CMB distribution is Gaussian. It is also expected that MEM will perform at least as well as WF since it has been shown that the entropic prior tends to the Gaussian one in the small fluctuation limit (Hobson et al. 1998). Thus, it is not surprising that both methods perform equally well when the underlying CMB is Gaussian. However, for non-Gaussian fields MEM would tend to perform better than WF. This is the case for our simulations since we find that the level of detection of intrinsic non-Gaussianity is, in general, slightly higher for the MEM reconstructions than for the ones obtained with WF. Although for the considered cases the differences between both reconstructions are small, they could be more important for other type of non-Gaussianity. For instance, Hobson et al. (1998) also show that the thermal SZ cluster profiles reconstructed with MEM are closer to the true ones than those obtained with WF. It is also interesting to note that, provided that we assume a good knowledge of the spectral behaviour of the Galactic foregrounds, their effect in the MEM and WF reconstructions is quite small. In fact, we have obtained our results for four different sets of Galactic foregrounds and found that the CMB reconstructions are quite insensitive to the input foreground maps. Regarding the LCFC technique, it produces lower non-Gaussian detections levels than both MEM and WF. We also find that, provided that we choose frequency channels which are relatively clean from Galactic foregrounds, the results do not depend on the chosen Galactic region (outside a Galactic cut with  $|b| = 20^\circ$ ). This result is confirmed by the tests performed in section 6.1, where only the thermal dust seems to be playing a role at the highest frequency channels. However, one should bear in mind that we are considering only small patches of the sky and that the foregrounds are expected to be more important at large scales. In addition, our simulated templates are subject to uncertainties that can be especially important at subdegree scales. We should also point out that, although our wavelet technique has not been able to pick the presence of fore-

ground residuals, other type of studies (e.g. phase analyses) may be more sensitive to the presence of foreground contamination.

The fact that MEM and WF provide better reconstructions than the LCFC is expected since MEM and WF are very powerful methods which make use of all the information present in the data to separate all the components. In addition, they try to deconvolve and to denoise the signal, what clearly improves our ability to recover the CMB. However, they require some important assumptions which can make the method less robust. On the contrary, the assumptions required by the LCFC are less strong. When using MEM and WF, the frequency dependence of all the components is assumed to be known. This is valid for the CMB, kinetic and thermal SZ effects but is only approximated for the Galactic foregrounds. Moreover the Galactic foregrounds are assumed to have a pixel independent spectral index, which may be a reasonable approximation for small patches of the sky (as the ones considered here) but it does not hold when considering large fractions of the sky. In addition, the results previously presented have been obtained assuming full knowledge of the power spectra and cross-correlations between the different components for both MEM and WF, although this assumption can be relaxed.

For small patches of the sky, one could try to obtain directly from the data the spectral behaviour of the foregrounds (assuming that it is spatially invariant). This could be done, for instance, by applying a blind-source separation method. Then this information could be included in the MEM (or WF) algorithm to perform the final reconstruction. Another solution is to use the extension of MEM recently developed by Stolyarov et al. (2005), which successfully accommodates spatially dust temperature variations. They find that the quality of the CMB reconstruction is comparable to the one obtained in the ideal case, when the dust temperature was assumed to be constant over the sky. The method can also be used to deal with other foregrounds.

With regard to the influence of the assumed power spectra, we have repeated the analysis using MEM assuming neither knowledge of the power spectra nor of the cross-correlations between the components. When the input temperature distribution is Gaussian, the reconstructed CMB map is again compatible with Gaussianity. For the non-Gaussian cases, the level of the detections are decreased. For the map with Gaussian:non-Gaussian proportion of 1:1, the highest non-Gaussian detection goes down to  $\sim 10\sigma$  (versus  $\sim 16.5\sigma$  when full information was used) and for the proportion 2:1, there is no detection outside the 99 per cent acceptance region. Similar qualitative results are found for WF, although with lower levels of detection for the 1:1 non-Gaussian map (the highest detection is at the  $\sim 7\sigma$  level). Note that these levels of detections are slightly below the ones obtained with the LCFC method. However, some information about the power spectra of the microwave components is already available and more is expected to be obtained from the current and future microwave experiments. Therefore a realistic situation would fall somewhere between the two cases presented here (full information and no information).

With regard to the LCFC, although the method is in principle less powerful than MEM and WF, it has the advantage of not requiring so strong assumptions about the

underlying signals. First of all we would need to have some reasonably good templates for the Galactic components at each considered frequency channel in order to be able to subtract the Galactic foreground contamination down to a 10 per cent. Given that Planck will take observations in a very large range of frequencies (30 to 857 GHz), including some channels to monitor Galactic foregrounds, this seems a plausible assumption. In any case, we have also repeated our analysis for the LCFC without subtracting any correction for the Galactic foregrounds and the results obtained were very similar to the ones presented here. Therefore, even if we were unable to reduce the Galactic contamination by a factor of 10, the method would still perform similarly well. The second and most important requirement to construct the LCFC is a good knowledge of the properties of the noise, which is also a reasonable assumption for the Planck satellite.

However, the choice of the channels to be combined is an important issue that must be studied in detail. For the present work, we have tried many different combinations of data maps and finally chosen to present our results with the combination of the 143 and 217 GHz channels. These two channels are relatively clean from Galactic contamination (which ensures that the amount of spurious non-Gaussianity introduced in the reconstructed CMB is very limited) and have a good resolution (important if we are looking for a non-Gaussian signal present at small scales). From all the tested combinations that preserved the Gaussian character of the CMB for the four considered regions of the sky (when the input was Gaussian), this was the one that yielded the highest non-Gaussian detections (when the input was non-Gaussian). We would like to remark that the optimal choice of channels will depend on the area of the sky that is being analysed as well as on the type of non-Gaussianity that we are trying to find. For instance, the 353 GHz channel has a good resolution but it may also have a high contamination from dust emission. However, if we are studying a particularly clean region of the sky, it can be helpful to add the 353 GHz channel. Also, if we are interested in looking for non-Gaussian signatures at larger scales we could instead add other channels (e.g. the 100 GHz map). This would reduce the resolution of the recovered CMB map, but it will increase the signal-to-noise ratio at the scales of interest. In addition, the optimal choice may also depend on the particular test that is used to study the temperature distribution.

We also have to point out that the proportion of cosmic strings (or other topological defects) present in the universe, if any, is uncertain. According to Bouchet et al. (2001), the best fit of a mixture of inflation and cosmic strings to the CMB power spectrum obtained from BOOMERanG (and other CMB experiments) yields to a string contribution of 18 per cent (in the power spectrum). This corresponds approximately to a mixture of Gaussian CMB and cosmic strings in proportion 2:1 in rms. Using the WMAP and 2dF data, Pogosian et al. (2003) conclude that a cosmic-string contribution  $\lesssim 10$  per cent can not be ruled out. If the cosmic strings proportion was lower than the cases studied in this work, the wavelet technique would not be able to detect this contribution with the reconstructed methods that we have considered. However, note that we are using small patches of the sky of size  $12.8^\circ \times 12.8^\circ$  for the analysis. But Planck will provide with all-sky observations of the microwave sky and thus it is expected that the non-Gaussian analysis can be

performed over a much larger fraction of the sky. Of course having a larger sky area implies that the proportion of cosmic strings that can be detected is also appreciably lower. Therefore we expect to obtain qualitatively similar results to the ones found in this work for non-Gaussian maps with lower proportions of cosmic strings that cover larger fractions of the sky.

To understand better the effect of the different contaminants on the CMB reconstruction, the results in sections 5.1 and 5.2 were obtained from simulated data that did not include the emission of point sources. In section 5.3 we repeat the non-Gaussianity analysis including point source emission for an input Gaussian CMB map. In particular, we perform the CMB reconstruction using MEM and a MEM+MHW joint analysis. We find that, when using only MEM, point source residuals contaminate the reconstructed CMB which clearly shows up in the wavelet statistic. However, this problem is solved when using the MEM+MHW joint analysis. Therefore using a tool such as the MHW to remove the brightest point sources prior to applying a component separation technique is crucial in order to avoid that spurious non-Gaussianity is present in the reconstructed CMB map. Again, when considering a larger fraction of the sky, we may wonder if we would be able to see the point source residuals. As shown in section 6.3, we do expect to see the residuals left by this contaminant when analysing a large fraction of the sky, even after subtracting the brightest point sources. Therefore it is a critical issue to either remove or mask as much as possible the contribution coming from this contaminant.

## 8 CONCLUSIONS

The aim of this work was to show the importance of considering the whole component separation process when testing the performance of statistical tools for Gaussianity analysis. The method used to reconstruct the CMB map may introduce or erase non-Gaussianity on the cosmological signal and it is very important to understand this effect in order to give a correct interpretation of the results of the analysis. This type of study also allows one to establish which reconstruction technique is better, not in the sense of recovering the best power spectrum, but with regard to preserve the underlying CMB temperature distribution.

In particular, we use a wavelet based technique to test the CMB recovered by three different methods: MEM, WF and LCFC. For the test we have used Planck simulated data on small patches of the sky, considering Gaussian and non-Gaussian CMB maps. Assuming that point sources have been appropriately removed, none of the methods seem to include spurious non-Gaussianity. However, when the underlying CMB is non-Gaussian, the three methods produce CMB reconstructions which are more Gaussian than the input one. This is mainly due to the presence of instrumental noise, which significantly affects the CMB reconstruction, especially at the smallest scales where the non-Gaussian signatures of our test maps were more important. MEM tends to provide slightly larger non-Gaussian detections than WF, whereas the detections are lower for the LCFC. This is mainly due to the fact that MEM and WF try to denoise

and deconvolve the signal and not so much to the fact that they remove better the foreground contamination.

When point sources are included, if no attempt to remove the brightest point sources is done, they clearly contaminate the CMB reconstructions introducing spurious non-Gaussianity. However, if we first apply the MHW to remove the brightest point sources, the reconstructions are again compatible with Gaussianity. This shows the importance of removing or masking the contamination coming from extragalactic point sources since otherwise it will impair our ability to detect intrinsic non-Gaussianity. Moreover, when considering a larger region of the sky, the point source residuals would be more statistically significant and we expect to detect them with our wavelet technique even after subtracting the brightest ones. Therefore we find that this is the most damaging contaminant for Gaussian analysis of the CMB, at least at the scales considered in this work and within the uncertainties of our foreground simulations (that could be more important at subdegree scales).

## ACKNOWLEDGEMENTS

RBB thanks the Ministerio de Ciencia y Tecnología and the Universidad de Cantabria for a Ramón y Cajal contract. The authors thank F.R.Bouchet, J.M.Diego and L.Toffolatti for kindly provide the cosmic strings, SZ and point source simulations, respectively. We thank the RTN of the EU project HPRN-CT-2000-00124 for partial financial support. RBB, EMG and PV acknowledge partial financial support from the Spanish MCYT project ESP2004-07067-C03-01 and from a joint Spain-France project (Acción Integrada HF03-163, Programmes d'Actions Intégrées (Picasso)).

## REFERENCES

- Acquaviva V., Bartolo N., Matarrese S., Riotto A., 2003, Nucl.Phys. B667 119-148
- Aghanim N., Forni O., 1999, A&A, 347, 409
- Aghanim N., Forni O., Bouchet F.R., 2001, A&A, 365, 341
- Aghanim N., Kunz M., Castro P.G., Forni O., 2003, A&A, 406, 797
- Aliaga A.M., Martínez-González E., Cayón L., Argüeso F., Sanz J.L., Barreiro R.B., Gallegos J.E., 2003, New Ast. Rev., 47, 907
- Aliaga A.M., Rubiño-Martín J.A., Martínez-González E., Barreiro R.B., Sanz J.L., 2005, MNRAS, 356, 1559
- Baccigalupi C., Bedini L., Burigana C., De Zotti G., Farusi A., Mairo D., Maris M., Perrota F., Salerno E., Toffolatti L., Tonazzini A., 2000, MNRAS, 318, 769
- Banday A.J., Gorski K.M., Bennett C.L., Hinshaw G., Kogut A., Lineweaver C., Smoot G.F., Tenorio L., 1997, ApJ, 475, 393
- Barreiro R.B., Sanz J.L., Martínez-González E., Silk J., 1998, MNRAS, 296, 693
- Barreiro R.B., Hobson M.P., Lasenby A.N., Banday A.J., Górski K.M., Hinshaw G., 2000, MNRAS, 318, 475
- Barreiro R.B., Martínez-González E., Sanz J.L., 2001, MNRAS, 322, 411
- Barreiro R.B., Hobson M.P., 2001, MNRAS, 327, 813
- Barreiro R.B., Sanz J.L., Herranz D., Martínez-González E., 2003, MNRAS, 342, 119
- Barreiro R.B., Hobson M.P., Banday A.J., Lasenby A.N., Stolyarov V., Vielva P., Górski K.M., 2004, MNRAS, 351, 515
- Barreiro R.B., 2006, proceedings of Data analysis in cosmology, Springer-Verlag Lecture Notes in Physics, eds V.J. Martínez, E. Martínez-González, M.J. Pons-Bordería and E. Saar, Valencia 6-10 September 2004, in press, preprint (astro-ph/0512538)
- Bartolo N., Komatsu E., Matarrese S., Riotto A., 2004, Phys.Rept., 402, 103
- Bedini L., Herranz D., Salerno E., Baccigalupi C., Kuruoglu E.E., Tonazzini A., 2005, EURASIP JASP in the Special Issue on "Applications of Signal Processing in Astrophysics and Cosmology", 15, 2400
- Bennett C.L. et al., 2003a, ApJS, 148, 1
- Bennett C.L. et al., 2003b, ApJS, 148, 97
- Benoit A. et al., 2003, A&A, 399, L19
- Bernardeau F., Uzan J.-P., 2002, Phys. Rev. D, 66, 103506
- Bouchet F.R., Bennett D.P., Stebbins A., 1988, Nat, 335, 410
- Bouchet F.R., Gispert R., Puget J.L., 1996, in Dwek E., ed., Proc. AIP Conf. 348. The mm/sub-mm foregrounds and future CMB space missions. AIP Press, New York, p.255
- Bouchet F.R., Gispert R., 1999, New Astr. Rev., 4, 443
- Bouchet F.R., Peter P., Riazuelo A., Sakellariadou M., 2001, Phys.Rev.D, 65, 021301
- Burrus C.S., Gopinath R.A., Guo H., 1998, 'Introduction to Wavelets and Wavelet Transforms. A primer', Prentice-Hall, Upper Saddle River, New Jersey
- Cabella P., Hansen F., Marinucci D., Pagano D., Vittorio N., 2004, Phys. Rev. D, 69, 3007
- Cabella P., Liguori M., Hansen F.K., Marinucci D., Matarrese S., Moscardini L., Vittorio N., 2005, MNRAS, 358, 684
- Cayón L., Sanz J.L., Barreiro R.B., Martínez-González E., Vielva P., Toffolatti L., Silk J., Diego J.M., Argüeso F., 2000, MNRAS, 315, 757
- Cayón L., Sanz J.L., Martínez-González E., Banday A.J., Argüeso F., Gallegos J.E., Górski K.M., Hinshaw G., 2001, MNRAS, 326, 1243
- Cayón L., Argüeso F., Martínez-González E., Sanz J.L., 2003a, MNRAS, 344, 917
- Cayón L., Martínez-González E., Argüeso F., Banday A.J., Górski K.M., 2003b, MNRAS, 339, 1189
- Cayón L., Jin J., Treaster A., 2005, MNRAS, 362, 826
- Chiang L.-Y., Jorgensen H.E., Naselsky I.P., Naselsky P.D., Novikov I.D., Christensen P.R., 2002, MNRAS, 335, 1054
- Chiang L.-Y., Naselsky P.D., Verkhodanov O.V., Way M.J., 2003, ApJ, 590, L65
- Chiang L.-Y., Naselsky P.D., 2004, MNRAS, submitted (astro-ph/0407395)
- Chiang L.-Y., Naselsky P., Coles P., 2004, ApJ, 602, L1
- Coles P., 1988, MNRAS, 234, 509
- Coles P., Barrow J.D., 1987, MNRAS, 228, 407
- Coles P., Dineen P., Earl J., Wright D., 2004, MNRAS, 350, 989
- Colley W.N., Gott J.R., 2003, MNRAS, 344, 686
- Copi C.J., Huterer D., Starkman G.D., 2004, PhRvD, 70, 043515

- Cruz M., Martínez-González E., Vielva P., Cayón L., 2005, MNRAS, 356, 29
- Daubechies I., 1992, 'Ten Lectures on Wavelets', S.I.A.M., Philadelphia
- de Zotti G., Ricci R., Mesa D., Silva L., Mazzotta P., Toffolatti L., González-Nuevo J., 2005, A&A, 431, 893
- Delabrouille J., Cardoso J.F., Patanchon G., 2003, MNRAS, 346, 1089
- Diego J.M., Martínez-González E., Sanz J.L., Mollerach S., Martínez V.J., 1999, 306, 427
- Diego J.M., Diego J.M., Martínez-González E., Sanz J.L., Cayón L., Silk J., 2001, MNRAS, 325, 1533
- Diego J.M., Vielva P., Martínez-González E., Silk J., Sanz J.L., 2002, MNRAS, 336, 1351
- Doré O., Colombi S., Bouchet F.R., 2003, MNRAS, 344, 905
- Durrer R., 1999, New Astron. Rev., 43, 111
- Eriksen H.K., Hansen F.K., Banday A.J., Górski K.M., Lilje P.B., 2004a, ApJ, 605, 14
- Eriksen H.K., Novikov D.I., Lilje P.B., Banday A.J., Górski K.M., 2004b, ApJ, 612, 64
- Eriksen H.K., Banday A.J., Górski K.M., Lilje P.B., 2004c, ApJ, 612, 633
- Ferreira P.G., Magueijo J., Górski K.M., 1998, ApJ, 503, L1
- Ferreira P.G., Magueijo J., Silk J., 1997, Phys. Rev. D, 56, 4592
- Finkbeiner D.P., Davis M., Schlegel D.J., 1999, ApJ, 524, 867
- Forni O., Aghanim N., 1999, A&AS, 137, 553
- Gaztañaga E., Wagg J., 2003, Phys. Rev. D, 68, 021302
- Gaztañaga E., Wagg J., Multamaki T., Montana A., Hughes D.H., 2003, MNRAS, 346, 47
- Giardino G., Banday A.J., Górski K.M., Bennett K., Jonas J.L., J. Tauber, 2002, A&A, 387, 82
- González-Nuevo J., Toffolatti L., Argüeso F., 2005, ApJ, 621, 1
- Gott III J.R., Park C., Juszkievicz R., Bies W.E., Bennett D.P., Bouchet F.R., Stebbins A., 1990, ApJ, 352, 1
- Grainge K. et al., 2003, MNRAS, 341, L23
- Halverson W., et al., 2002, ApJ, 568, 38
- Hanany S., et al. 2000, ApJ, 545, L5
- Hansen F.K., Cabella P., Marinucci D., Vittorio N., 2004, ApJ, 607, L67
- Heavens A.F., 1998, MNRAS, 299, 805
- Heavens A.F., Sheth R.K., 1999, MNRAS, 310, 1062
- Herranz D., Sanz J.L., Hobson M.P., Barreiro R.B., Diego J.M., Martínez-González E., Lasenby A.N., 2002a, MNRAS, 336, 1057
- Herranz D., Gallegos J., Sanz J.L., Martínez-González E., 2002b, MNRAS, 334, 533
- Herranz D., Sanz J.L., Barreiro R.B., Martínez-González E., 2002c, ApJ, 580, 610
- Herranz D., Sanz J.L., Barreiro R.B., López-Caniego M., 2005, MNRAS, 356, 944
- Hobson M.P., Jones A.W., Lasenby A.N., Bouchet F.R., 1998, MNRAS, 300, 1
- Hobson M.P., Barreiro R.B., Toffolatti L., Lasenby A.N., Sanz J.L., Jones A.W., Bouchet F.R., 1999a, MNRAS, 306, 232
- Hobson M.P., Jones A.W., Lasenby A.N., 1999b, MNRAS, 309, 125
- Hobson M.P., McLachlan C., 2003, MNRAS, 338, 765
- Kogut A., Banday A.J., Bennett C.L., Górski K., Hinshaw G., Smoot G.F., Wright E.L., 1996, ApJ, 464, L29
- Komatsu E. et al., 2003, ApJS, 148, 119
- Kuo C.L. et al., 2004, ApJ, 600, 32
- Land K., Magueijo J., 2005, MNRAS, 357, 994
- Larson D.L., Wandelt B.D., 2004, ApJ, 613, L85
- Linde A., Mukhanov V., 1997, Phys. Rev., D56, 535
- López-Caniego M., Herranz D., Barreiro R.B., Sanz J.L., 2004, SPIE, 5299, 145
- López-Caniego M., Herranz D., Barreiro R.B., Sanz J.L., 2005a, MNRAS, 359, 993
- López-Caniego M., Herranz D., Sanz J.L., Barreiro R.B., 2005b, EURASIP Journal on Applied Signal Processing, 15, 1
- Magueijo J., 2000, ApJ, 528, L57
- Magueijo J., Medeiros J., 2004, MNRAS, 351, L1
- Maino D., Farusi A., Baccigalupi C., Perrotta F., Banday A.J., Bendini L., Burigana C., De Zotti G., Górski K.M., Salerno, E., 2002, MNRAS, 334, 53
- Maino D., Banday A.J., Baccigalupi C., Perrotta F., Górski K.M., 2003, MNRAS, 344, 544
- Mallat S.G., 1989, IEEE Trans. Acoust. Speech Sig. Proc., 37, 2091
- Martínez-González E., Barreiro R.B., Diego J.M., Sanz J.L., Cayón L., Silk J., Mollerach S., Martínez V.J., 2000, ApL&C, 37, 335
- Martínez-González E., Gallegos J.E., Argüeso F., Cayón L., Sanz J.L., 2002, MNRAS, 336, 22
- Martínez-González E., Diego J.M., Vielva P., Silk J., 2003, MNRAS, 345, 1101
- Mason B.S. et al., 2003, ApJ, 591, 540
- McEwen J.D., Hobson M.P., Lasenby A.N., Mortlock D.J., 2005, MNRAS, 359, 1583
- Melin J.-B., Bartlett J.G., Delabrouille J., 2005, A&A, 429, 417
- Monteserín C., Barreiro R.B., Sanz J.L., Martínez-González E., 2005, MNRAS, 360, 9
- Mukherjee P., Hobson M.P., Lasenby A.N., 2000, MNRAS, 318, 1157
- Mukherjee P., Wang Y., 2004, ApJ, 613, 51
- Naselsky P., Novikov D., 1995, ApJ, 444, L1
- Netterfield C.B., et al., 2002, ApJ, 571, 604
- Pando J., Valls-Gabaud D., Fang L.-Z., 1998, Phys. Rev. Lett., 81, 4568
- Park C.G., 2004, MNRAS, 349, 313
- Patanchon G., Cardoso J.F., Delabrouille J., Vielva P., 2005, MNRAS, 364, 1185
- Peebles P. J. E., 1997, ApJ, 483, 1
- Pierpaoli E., 2003, ApJ, 589, 58
- Pierpaoli E., Anthoine S., Huffenberger K., Daubechies I., 2005, MNRAS, 359, 261
- Pogosian L., Henry Tye S.-H., Wasserman I., Wyman M., 2003, Phys. Rev. D., 68, 023506
- Pompilio M.P., Bouchet F.R., Murante G., Provenzale A., 1995, ApJ, 449, 1
- Rybicki G.B., Press W.H., 1992, ApJ, 398, 169
- Sanz J.L., Herranz D., Martínez-González E., 2001, ApJ, 552, 484
- Schaefer B.M., Pfrommer C., Hell R., Bartelmann M., 2004, MNRAS, submitted; preprint (astro-ph/0407090)
- Schulz A.E., White M., 2003, ApJ, 586, 723

- Schwarz D.J., Starkman G.D., Huterer D., Copi C.J., 2004, Phys.Rev.Lett., 93, 221301
- Seljak U., Zaldarriaga M., 1996, ApJ, 469, 437
- Stolyarov V., Hobson M.P., Lasenby A.N., Barreiro R.B., 2005, MNRAS, 357, 145
- Stolyarov V., Hobson M.P., Ashdown M.A.J., Lasenby A.N., 2002, MNRAS, 336, 97 (S02)
- Tegmark M., de Oliveira-Costa A., 1998, ApJ, 500, 83
- Tegmark M., de Oliveira-Costa A., Hamilton A.J.S., 2003, Phys. Rev. D, 68, 123523
- Tegmark M., Efstathiou G., 1996, MNRAS, 281, 1297
- Toffolatti L., Argüeso-Gómez F., de Zotti G., Mazzei P., Franceschini A., Danese L., Burigana C., 1998, MNRAS, 297, 117
- Turok N., Spergel D. N., 1990, Phys. Rev. Letters, 64, 2736
- Vielva P., Martínez-González E., Cayón L., Sanz J.L., Toffolatti L., 2001a, MNRAS, 326, 181
- Vielva P., Barreiro R.B., Hobson M.P., Martínez-González E., Lasenby A.N., Sanz J.L., Toffolatti L., 2001b, MNRAS, 328, 1
- Vielva P., Martínez-González E., Gallegos J.E., Toffolatti L., Sanz J.L., 2003, MNRAS, 344, 89
- Vielva P., Martínez-González E., Barreiro R.B., Sanz J.L., Cayón L., 2004, ApJ, 609, 22
- Wiaux Y., Jacques L., Vanderghynst P., 2005a, ApJ, 632, 15
- Wiaux Y., Jacques L., Vanderghynst P., 2005b, ApJ, submitted, preprint (astro-ph/0508516)